Solar Phys (2013) 285:317–348
DOI 10.1007/s11207-013-0260-5

Heliospheric Imaging of 3D Density Structures During the Multiple Coronal Mass Ejections of Late July to Early August 2010

D.F. Webb · C. Möstl · B.V. Jackson · M.M. Bisi · T.A. Howard · T. Mulligan · E.A. Jensen · L.K. Jian · J.A. Davies · C.A. de Koning · Y. Liu · M. Temmer · J.M. Clover · C.J. Farrugia · R.A. Harrison · N. Nitta · D. Odstrcil · S.J. Tappin · H.-S. Yu

Received: 28 February 2012 / Accepted: 23 February 2013 / Published online: 23 April 2013

Abstract It is usually difficult to gain a consistent global understanding of a coronal mass ejection (CME) eruption and its propagation when only near-Sun imagery and the local measurements derived from single-spacecraft observations are available. Three-dimensional (3D) density reconstructions based on heliospheric imaging allow us to "fill in" the temporal and spatial gaps between the near-Sun and *in situ* data to provide a truly global picture of the

Observations and Modelling of the Inner Heliosphere
Guest Editors: Mario M. Bisi, Richard A. Harrison, and Noé Lugaz

Electronic supplementary material The online version of this article (doi:10.1007/s11207-013-0260-5) contains supplementary material, which is available to authorized users.

D.F. Webb (✉)
Institute for Scientific Research, Boston College, Chestnut Hill, MA, USA
e-mail: david.WEBB@hanscom.af.mil

C. Möstl · M. Temmer
Institute of Physics, University of Graz, Graz 8010, Austria

C. Möstl · Y. Liu
Space Sciences Laboratory, University of California, Berkeley, CA, USA

B.V. Jackson · J.M. Clover · H.-S. Yu
Center for Astrophysics and Space Science, University of California, San Diego, La Jolla, CA, USA

M.M. Bisi
Institute of Mathematics and Physics, Aberystwyth University, Aberystwyth, Ceredigion, Wales, UK

T.A. Howard
Southwest Research Institute, Boulder, CO, USA

T. Mulligan
Space Sciences Dept/SSAL, The Aerospace Corporation, Los Angeles, CA, USA

E.A. Jensen
ACS Consulting, 40 FM 1960 W PMB 370, Houston, TX, USA

propagation and interactions of the CME as it moves through the inner heliosphere. In recent years the heliospheric propagation of dense structures has been observed and measured by the heliospheric imagers of the *Solar Mass Ejection Imager* (SMEI) and on the twin *Solar TErrestrial RElations Observatory* (STEREO) spacecraft. We describe the use of several 3D reconstruction techniques based on these heliospheric imaging data sets to distinguish and track the propagation of multiple CMEs in the inner heliosphere during the very active period of solar activity in late July – early August 2010. We employ 3D reconstruction techniques used at the University of California, San Diego (UCSD) based on a kinematic solar wind model, and also the empirical Tappin–Howard model. We compare our results with those from other studies of this active period, in particular the heliospheric simulations made with the ENLIL model by Odstrcil *et al.* (*J. Geophys. Res.*, 2013) and the *in situ* results from multiple spacecraft provided by Möstl *et al.* (*Astrophys. J.* **758**, 10 – 28, 2012). We find that the SMEI results in particular provide an overall context for the multiple-density flows associated with these CMEs. For the first time we are able to intercompare the 3D reconstructed densities with the timing and magnitude of *in situ* density structures at five spacecraft spread over 150° in ecliptic longitude and from 0.4 to 1 AU in radial distance. We also model the magnetic flux-rope structures at three spacecraft using both force-free and non-force-free modelling, and compare their timing and spatial structure with the reconstructed density flows.

1. Introduction

On 1 August 2010 multiple CMEs erupted from the Earth-facing side of the solar disk. Prior to 1 August, several mid-latitude active regions had developed, but around 1 August there was a rapid increase in magnetic complexity and associated activity, involving a number

L.K. Jian
Heliophysics Science Division, Code 672, NASA Goddard Space Flight Center, Greenbelt, MD, USA

L.K. Jian
Department of Astronomy, University of Maryland, College Park, MD, USA

J.A. Davies · R.A. Harrison
RAL Space, Harwell Oxford, Didcot, Oxfordshire, England, UK

C.A. de Koning
NOAA Space Weather Prediction Center, Boulder, CO, USA

C.J. Farrugia
Space Science Center and Department of Physics, University of New Hampshire, Durham, NH, USA

N. Nitta
Solar and Astrophysics Laboratory, Lockheed Martin Advanced Technology Centre, Palo Alto, CA, USA

D. Odstrcil
Department of Computational and Data Sciences, George Mason University, Fairfax, VA, USA

D. Odstrcil
NASA Goddard Space Flight Center, Greenbelt, MD, USA

S.J. Tappin
National Solar Observatory, Sacramento Peak, Sunspot, NM, USA

of prominence eruptions, small flares, and quite rapid magnetic development apparently involving regions on the solar surface separated by tens of heliodegrees (*e.g.*, Schrijver and Title, 2011). This was the first time in the current solar cycle when multiple events were observed remotely by coronagraphs and the heliospheric imagers of the *Solar Mass Ejection Imager* (SMEI) in Earth orbit (Eyles *et al.*, 2003; Jackson *et al.*, 2004), and on-board the twin STEREO (*Solar TErrestrial RElations Observatory*) spacecraft in ~ 1 AU solar orbits (Kaiser *et al.*, 2008; Eyles *et al.*, 2009; Harrison *et al.*, 2012). These CMEs were associated with flares and filament eruptions in different regions of the northern solar hemisphere as described in detail by Schrijver and Title (2011) based on observations from the NASA *Solar Dynamics Observatory* (SDO) satellite. The surface activity associated with some of these CMEs have been analysed and modelled by Li *et al.* (2011) and Liu *et al.* (2010c) and simulated in three-dimensions as magnetically coupled eruptions by Török *et al.* (2011).

These eruptions, along with several occurring in late July and early August, resulted in a complex pattern of single and multiple interacting plasma and magnetic structures in the inner heliosphere. Subsequently, Harrison *et al.* (2012) used primarily the STEREO *Sun Earth Connection Coronal and Heliospheric Investigation* (SECCHI) *Heliospheric Imager* (HI) images to identify and understand the propagation and evolution of the CMEs associated with this activity as they traversed the low solar corona through the inner heliosphere out to distances beyond 1 AU. These authors also used data from a number of other instruments making coronal and heliospheric observations of the CMEs, and applied a variety of techniques to achieve a consistent picture of the events, particularly those that were Earth-directed. The SECCHI package on each STEREO spacecraft comprises the EUV Imager (EUVI), two coronagraphs (COR1 and COR2), and the HI instruments, HI-1 and HI-2 (Howard *et al.*, 2008). At the time STEREO-B was located 71.2° east of, and STEREO-A 78.3° west of, the Earth, as illustrated by Figure 1 (from Möstl *et al.*, 2012).

Although the events during this period were well-observed by various remote and *in situ* instruments, it was sometimes difficult to isolate the effect of individual features on the geospace environment and to identify their signatures at the various spacecraft. A series of workshops on these events were organised in Abingdon, England, Graz, Austria, and Aberystwyth, Wales, and the results of the analyses have been published in a series of papers including i) the underlying solar magnetic evolution – Schrijver and Title (2011), ii) "J-map" tracking analysis using the STEREO HI data and linking to source regions – Harrison *et al.* (2012), iii) CME-CME interactions – Liu *et al.* (2012) and Temmer *et al.* (2012), iv) impacts in the heliosphere observed *in situ* by the *Wind*, STEREO, *Venus Express* (VEX), *and MErcury Surface, Space ENvironment, GEochemistry, and Ranging* (MESSENGER – Domingue and Russell, 2007) spacecraft – Möstl *et al.* (2012), and v) numerical simulations using the ENLIL model – Odstrcil *et al.* (2013). We are aware of two other 3D simulations of the 1 August events, using the HAFv.2 kinematic model (Zhang *et al.*, 2013) and the "HAFv.2 + 3DMHD" hybrid model (Wu *et al.*, 2011). However, these latter simulations were restricted to the two Earth-directed CMEs early on 1 August.

In this paper we complement these efforts by analyses of these events obtained from a 3D reconstruction of heliospheric density from remote-sensing observations by heliospheric imagers. This effort is important because the properties of CMEs can be significantly modified during their initial development in the corona and propagation through the heliosphere because of interactions both with the structured background solar wind and with other CMEs launched during particularly active periods such as during July – August 2010. Therefore, it is difficult to predict their arrival and impact at spacecraft and planets using near-Sun observations only. *In situ* measurements at spacecraft can provide detailed plasma and magnetic field measurements of CMEs and constrain models of their propagation, but due to

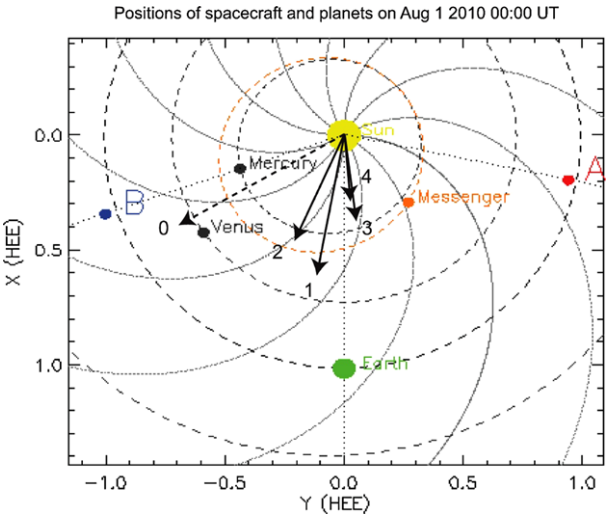

Figure 1 Ecliptic plane view of the location in Heliocentric Earth Ecliptic (HEE) coordinates on 1 August 2010, 00:00 UT, of observation sites at spacecraft at STEREO A, B, the Earth (L_1), Venus (VEX), and MESSENGER, and of the inner planets Earth, Venus, and Mercury and their orbits (dashed lines – note that MESSENGER was not in orbit at Mercury). The outermost orbit is that of Mars, which at this time was outside of the plot toward the upper left. The CMEs propagated mostly within the region bounded by STEREO-A (A) and STEREO-B (B), which were 150° apart. The arrows indicate the initial directions of CMEs 0 – 4 derived by Odstrcil *et al.* (2013) with an elliptical flux-rope model fitted to stereoscopic STEREO COR2 data. The dashed arrow indicates the 30 July CME not discussed by Harrison *et al.* (2012). The lengths of the arrows are a rough guide to the launch sequence of the CMEs, with shorter arrows indicating later launches. Plot adapted from Möstl *et al.* (2012), Figure 1a.

large spatial distances and the limited number of spacecraft, it is difficult to understand the 3D structure of CMEs from solar observations and *in situ* measurements alone. It is now clear that remote-sensing by heliospheric imagers can play an important role in studying the heliospheric propagation and evolution of CMEs.

An important difference between heliospheric imagers and coronagraphs is that some 3D information, such as the structure and kinematics of CMEs, is better characterised in heliospheric imaging than in coronagraph data. This is because the assumptions imposed on coronagraphs, such as skyplane and small-angle assumptions, are less valid at large elongations and across large distances, and heliospheric imagers observe extended CME evolution including interactions with the solar wind. However, analysing these observations is difficult because the appearance of the white-light structures combines effects of the 3D density structure and its varying distance to the Thomson surface (*e.g.*, Howard, 2011). Theory, modelling, and simulations involving heliospheric imaging capabilities have been developed by Jackson *et al.* (2006, 2010a, 2011), Vourlidas and Howard (2006), Kahler and Webb (2007), and Howard and Tappin (2009). Recent papers that consider the 3D structure of CMEs include Davies *et al.* (2009), Davis *et al.* (2009), Möstl *et al.* (2009c, 2010), Wood and Howard (2009), Lugaz, Vourlidas, and Roussev (2009), Lugaz *et al.* (2010), Howard and Tappin (2009, 2010), Liu *et al.* (2010a, 2010b, 2011), Wood, Howard, and Socker (2010), and Jackson *et al.* (2010a). See also recent reviews of techniques involving the extraction of 3D properties from heliospheric image data by Mierla *et al.* (2010), Howard (2011), and Rouillard (2011).

Even though the CMEs can be observed by coronagraphs, traced by heliospheric imagers, and detected *in situ* by various spacecraft, it can still be difficult to obtain a "global picture"

and associate individual events and evaluate their contributions to geospace effects using these observations alone. Therefore, numerical heliospheric simulations are also important both for predicting arrivals and impacts, and for analysing remote observations and *in situ* measurements.

This paper is organised as follows: Section 2 provides an overview of the instrumentation available and the resulting observations and measurements made during this period, with emphasis on the *in situ* and heliospheric aspects. Section 3 is an overview of the solar and low coronal observations and of the *in situ* measurements. In Section 4 we discuss how we connect the solar and heliospheric aspects of the CMEs, using the heliospheric imaging density reconstructions and the ENLIL simulations. We summarise and conclude in Section 5. Three movies are included as supplementary material for the online version. M1 compares the timing of transient density flows from 29 July through 8 August 2010 of the HI-1A and HI-2A images (top) with the proton density from the *Wind* spacecraft at the Sun–Earth Lagrange point L_1 (bottom). M2 is a movie of high-resolution SMEI 3D density reconstruction images in the ecliptic plane run with a constant solar wind velocity of 650 $\mathrm{km\,s^{-1}}$ during the 30 July – 7 August 2010 period. M3 is a movie of the same reconstruction images but in a meridional plane that includes the Sun, the Earth, and the ecliptic poles. The techniques used for making the movies are described later.

2. Overview of Heliospheric *in situ* Measurements and Remote-Sensing Observations Available in August 2010

Möstl *et al.* (2012) summarised the locations and *in situ* data available during this period, and the shocks and magnetic structures, including flux ropes that were observed at five spacecraft locations. Figure 1, adapted from their paper, provides an ecliptic plane view of the locations on 1 August, 00:00 UT, of spacecraft, the inner planets, and the approximate CME trajectories in ecliptic-plane projection (from Odstrcil *et al.*, 2013), with shorter arrows indicating later origins. Fortuitously, the spacecraft were clearly separated in ecliptic longitude, and some in radial distance, yet all were within a few degrees of the ecliptic plane. The widest longitudinal separation between STEREO-B (radial distance, r, from the Sun of 1.06 AU and the farthest east) and STEREO-A ($r = 0.96$ AU and the farthest west) was 149.9° (HEE coordinates). The MESSENGER ($r = 0.38$ AU) and VEX (in orbit at Venus at $r = 0.73$ AU) spacecraft were in favourable positions, each lying between the longitudes of each STEREO spacecraft and *Wind*, which was located at the L_1 point sunward of the Earth ($r = 1.006$ AU, with the Earth at 1.015 AU) at the time. MESSENGER in its close orbit to the Sun moves much faster than the other spacecraft – from 1 – 4 August it moved radially from 0.40 to 0.37 AU and in longitude from 42.9 to 52.6°. The *Mars Express* and *Global Surveyor* probes were in orbit at Mars, but unfortunately obtained no solar wind data during this period. Mars was located to the east of the Sun–Earth line, at ∼98° longitude and 1.54 AU. During this period MESSENGER only obtained magnetic field data (Anderson *et al.*, 2007), and VEX obtained magnetic field data but no useful plasma data.

For context we now summarise the characteristics of the background solar wind observed at each of the 1 AU locations. We describe the *in situ* measurements and modelling of the CME activity, or lack of activity, at all five spacecraft locations below in Section 3.2. Figures 2 and 3 show the *in situ* parameters at STEREO-B and -A, respectively, for the first seven days in August. Both STEREO spacecraft revealed recurrent high-speed solar wind streams (HSSs) that peaked in early August at ∼600 – 700 $\mathrm{km\,s^{-1}}$. The HSS peak at STEREO-B occurred on 3 August and at STEREO-A on 4 August. The STEREO-B peak

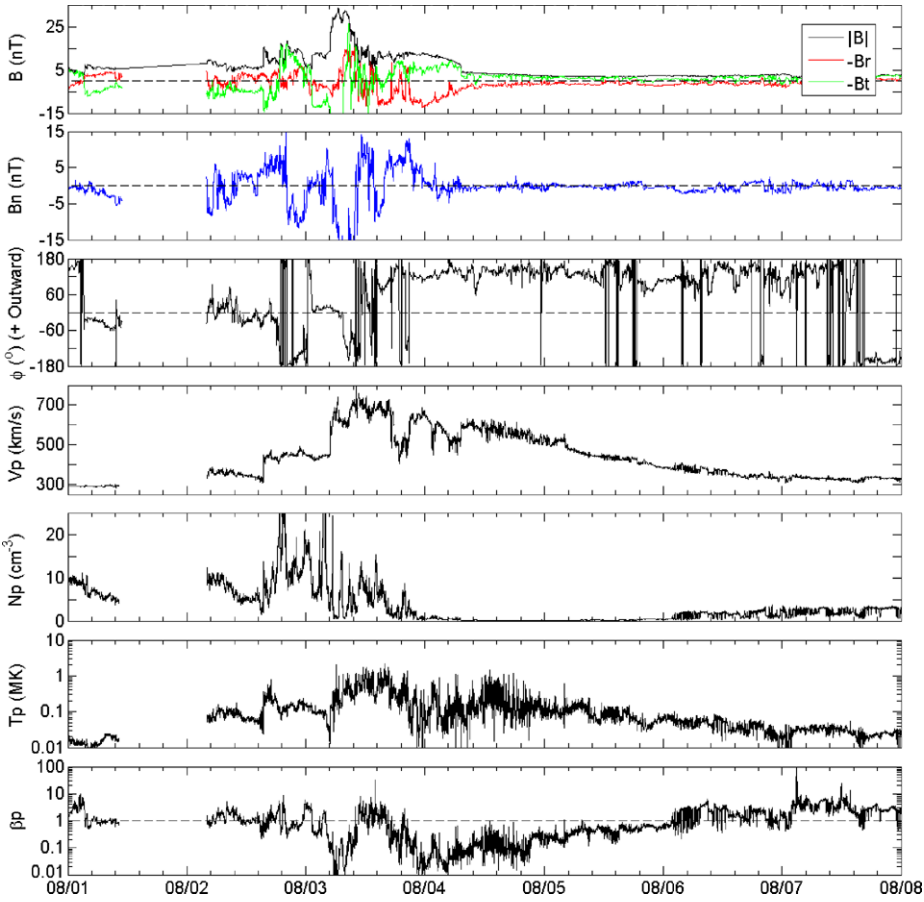

Figure 2 Seven-day plot of *in situ* parameters at STEREO-B 1 – 8 August 2010. The top plot shows the total magnetic field (black) and its radial (red) and tangential (green) components, and the second plot the normal (blue) component. The third plot gives the equivalent azimuthal angle $\phi = \text{atan}\,2(B_\text{r}, B_\text{t})$. When this angle is positive, the magnetic field is directed outward from the Sun, and when it is negative, it is inward-directed. The next three plots show the proton plasma parameters, V_n, N_p, and T_p, and the bottom plot is the plasma beta. This extended view shows that the HSS peaked at STEREO-B about one day earlier than at STEREO-A. A sector boundary crossing at STEREO-B from $B\phi$ inward to outward occurred on 3 August, ∼08:00, and was at the same general time as the onsets of the HSS, the shock S2, and CME M2.

was much sharper than the STEREO-A peak and most likely influenced by the CME activity there. The HSSs encountered at STEREO-B and STEREO-A were probably not the same stream because of the longitude spread and timing (see also the ENLIL simulations of Odstrcil *et al.*, 2013). Considering the observations at the two STEREO spacecraft and at L_1, a sector-boundary crossing was clearest at STEREO-B. The crossing is indicated by ϕ, the equivalent azimuthal angle of the interplanetary magnetic field, changing from inward toward the Sun to outward on 3 August, ∼08:00 UT, coincident not only with the HSS rise but also with the shock, S2, and enhanced magnetic field (described later). As noted by Crooker *et al.* (1993), Hundhausen (1993), and others, it is not unusual for CMEs to occur near sector boundaries since CMEs often arise from streamers that form the base of the heliospheric current sheet. Before the crossing the STEREO-B field direction was primarily inward.

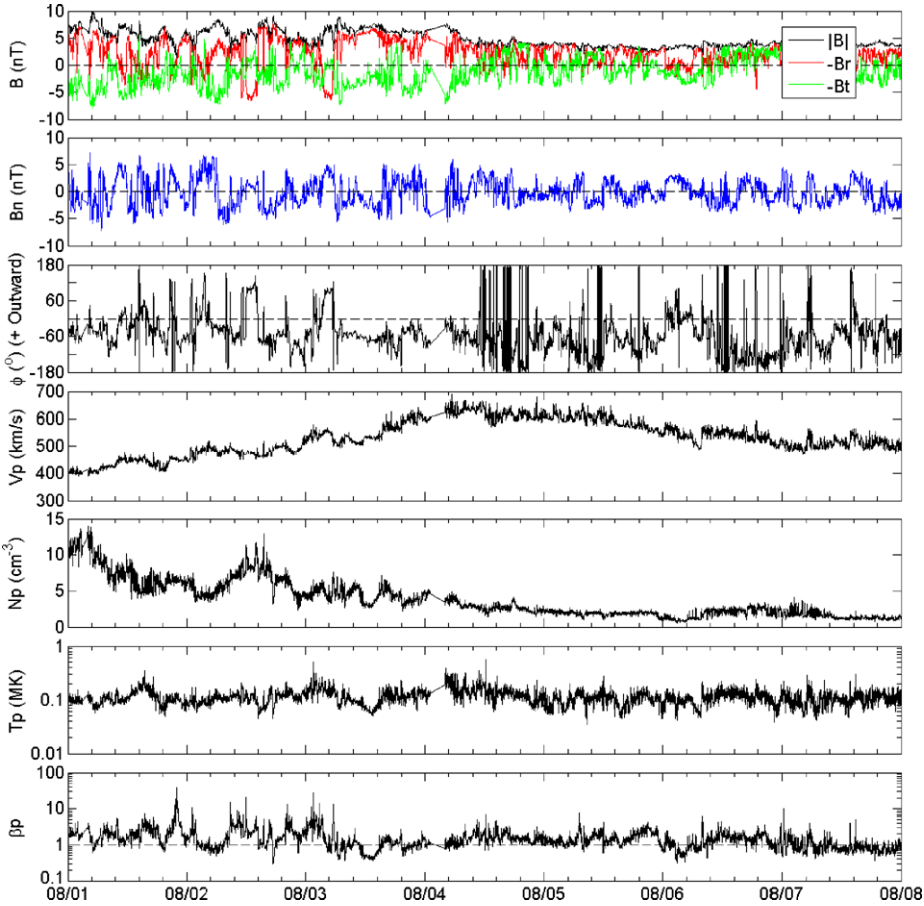

Figure 3 7-day plot of *in situ* parameters at STEREO-A 1 – 8 August 2010. The panels are the same as in Figure 2. Note the high-speed stream but lack of any obvious CME signatures during this period.

The *Wind* spacecraft was immersed in an inward-directed interplanetary magnetic field, *i.e.*, toward sector solar wind stream during the early August period but with strong fluctuations. Before this period a recurring HSS peaked at *Wind* at 700 km s^{-1} on 29 July and was declining through early August. This is probably the same HSS that peaked at STEREO-A six days later. Thus, during early August the Earth was immersed in slow solar wind, between the HSSs at the longitudes of STEREO-B and STEREO-A (see Odstrcil *et al.*, 2013). STEREO-A revealed no clear transient signatures during the first seven days of August (Figure 3). The proton density, N_p, at STEREO-A declined gradually during the HSS period in early August from a peak of $\sim$20 cm^{-3} in late July – early August.

The heliospheric propagation of the density structures associated with these multiple events were observed remotely by the heliospheric imagers from SMEI and on the twin STEREO spacecraft. In Earth orbit SMEI observed the entire sky beyond 20° elongation. The SECCHI HIs view the inner heliosphere in 1 AU solar orbits from elongations of 4 – 90° from the Sun and across a 90° range in position angle (PA). Together, the SECCHI telescopes provide a continuous view from the Sun to 1 AU and beyond. Furthermore, the stereoscopic viewpoints enable the possibility for 3D reconstruction using the coronagraphs and HIs.

All STEREO data were available during the August 2010 period, with the exception that STEREO-B data were not available from 1 August, 10:00 UT, until 2 August, 04:00 UT, due to an instrument outage.

3. Heliospheric Imaging: Connecting the CMEs at the Sun and in the Heliosphere

3.1. Summary of Solar and Coronal Observations of the CMEs

We used several 3D reconstruction techniques to try to understand the propagation of the plasma structures through the inner heliosphere, using their detection *in situ* by various spacecraft (Möstl *et al.*, 2012) to compare the trajectories and timing of the flows. The new aspects of this paper are the observations and 3D reconstruction modelling during this period of heliospheric density from the SMEI experiment, and comparison of these results with the other coordinated observations, especially with the *in situ* results at multiple spacecraft by Möstl *et al.* (2012) and the numerical magnetohydrodynamic (MHD) simulations of Odstrcil *et al.* (2013) .

Much of the Harrison *et al.* (2012) analysis is based on deriving "J-maps" from primarily the HI-1 and HI-2 STEREO-A images. Those authors focused their analysis on the four 1-August events and the kinematics/trajectories of those CMEs that might be Earth-impacting. Derivation of the propagation characteristics of the CMEs was based on the analysis of their time-elongation profiles (*e.g.*, Sheeley *et al.*, 1999; Rouillard *et al.*, 2008; Davies *et al.*, 2009; Tappin and Howard, 2009b; Liu *et al.*, 2010a, 2010b). J-maps show the locus of points along the lines-of sight from outward-moving structures, but not the solar distance of the structure at any given radius. The left panel of Figure 4 presents the J-map derived for 1 – 5 August from difference images from HI-1A and HI-2A that were discussed by Harrison *et al.* (2012). It has coloured dashed/dotted curves added that indicate the tracks corresponding to the four CMEs of 1 August: M = green, L = red, A = yellow, B = orange. Three of these tracks, L, A, and B, appear to extend all the way to the Earth (top of panel). The arrows in the same colours compare these CME tracks with the plasma and magnetic field data from the *Wind* spacecraft at L_1 for 3 – 6 August (right panel). The *Wind* panel shows the average arrival times at the Earth of tracks L, A, and B based on the CME speeds using several methods (see below).

Temmer *et al.* (2012) and Liu *et al.* (2012) also used these time-elongation profiles to study possible interactions/mergers involving CMEs M and L. In addition, Liu *et al.* (2012) and Odstrcil *et al.* (2013) analysed the track of an earlier CME on 30 July, which might have missed or grazed the Earth, but very likely impacted STEREO-B. In our general study we include these five CMEs and name them 0, 1, 2, 3, and 4. In Table 1a we provide the key information on these five CMEs and cross-reference the Harrison *et al.* (2012) and Liu *et al.* (2012) designations in column 5, as 'H/L', respectively. In addition, we add one more CME, called CME 5, that appeared late on 1 August. This CME was added because we see possible evidence of its heliospheric outflows in the SMEI density reconstructions that we discuss below. Thus, Table 1a consists of six CMEs with solar onsets ranging from 30 July to late on 1 August 2010. This extends the extraordinary amount of linked activity during this period that was first described by Schrijver and Title (2011).

Table 1a lists the timing and locations of the late July, early August 2010 CMEs. Column 1 lists the CME number; Column 2 the earliest CME onset time, here as observed by the STEREO COR1 coronagraphs; Column 3 the name of the surface activity associated with the onset and the onset time, usually taken from Harrison *et al.* (2012), and following Schrijver and Title (2011); Column 4 the GOES flare peak level, if any; Column 5 the

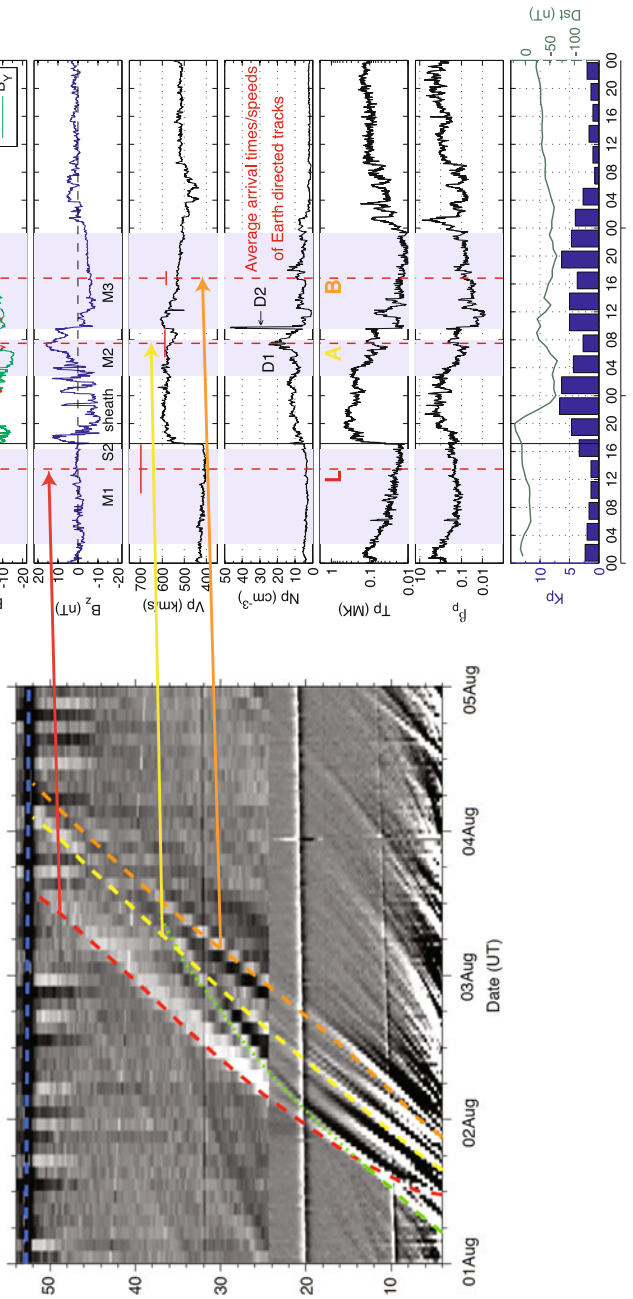

Figure 4 (Left) J-map derived for 1 – 5 August from STEREO-A HI-1 and HI-2 difference images and adapted from, and discussed in detail by, Harrison *et al.* (2012). The J-map is constructed along a PA of 85.2° chosen to correspond to that of the Earth (the ecliptic) as viewed from STEREO-A at the time of the observations. The near-horizontal signatures of Mercury, Venus, and the Earth can be seen in each panel at around 10, 20, and 53° elongation, respectively. The coloured dashed lines mark the M, L, A, and B CMEs, three of which appear to extend to the Earth at the top. The figure shows how the average arrival times based on the CME speeds using several methods of the three tracks, L, A, and B, might intercept the Earth; compare with (right) the plasma and magnetic field data from the *Wind* SWE (Ogilvie *et al.*, 1995) and MFI (Lepping *et al.*, 1995) experiments at L_1 and the K_p and *Dst* geoindices (bottom) for 3 – 6 August (from Möstl *et al.*, 2012).

Table 1 (a) Timing and locations of the late-July and early-August 2010 CMEs. (b) Timing and trajectories in heliosphere of the late-July and early-August 2010 CMEs.*

(a)

CME No.	CME onset (Date, UT) Instrument	Onset activity Onset (Date, UT)	Main flare GOES pk. Location	J-map track name H	J-map track name L	Source Long. SEL (°) Activity Type	J-map dir. SEL H	J-map dir. SEL L (°)	1 AU Direction	J-map: 1 AU arrival time (Date, UT), H	Peak *in situ* density (Date, UT)
				Onset (Date, UT), H							
0	7/30, 08:30 COR1A, 1B	Flare 0 30, 07:30(L)	? (N16E58)	–	1	E70 halo CME (ST-B)	–	30E	VEX, STEREO-B	–	3, 07:00 STEREO-B
1	8/1, 03:10 COR1A	Flare 1/Fil 0 1, 02:40(H)	B4.5 –	M	2	E10	(12-30E)	23E	?	(3, 12:30)	
2	8/1, 07:50 COR1A	Flare 2 1, 07:23(H)	C3.2 N19E34	L 1, 03:42 – 04:55	3	E36	3-36E	19E	L_1/Earth	3, 03:30 – 12:57	4, 07:00 *Wind*
3	8/1, 08:11 COR1A, 1B	Fil 1 1, 06:30(H)	(B3.0) –	A? 1, 10:45 – 11:05	–	W15 N-most fil.	4W-25E	–	L_1/Earth?	3, 22:00 – 4, 05:50	4, 09:30 *Wind*
4	8/1, 16:40 COR1A	Fl/Fil 2 1, 16:08(H)	B4.1 –	B 1, 15:10 – 17:49	–	W40 sm. W fil.	12E-24W	–	bet. Earth & STEREO-A?, MESSENGER?	4, 11:06 – 17:48	– STEREO-A
5	8/1, 21:40 COR1A	Fil 3 1, 18:00(H)	– –	–	–	W10 S-most fil.	–	–	?	–	4, 0600? SMEI

Table 1 (*Continued.*)

(b)

CME ID			VEX			STEREO-B			*Wind*			MESS			SMEI		
No.	H	L	Shock	Density increase	MFR	Shock	Density increase	MFR	Shock	Density increase	MFR	Shock	Density increase	MFR	CME No. *In situ* dens. Pk; Range time	SEL dir. S/C	Leading edge at 1 AU
0	–	1	S1 8/1, 14:41	–	M1	S1 8/2, 15:30	Y 8/2, 19 8/2, 20	M1	–	No	M1	–	–	M1 8/2, 14:12	SM0 8/3, 06 8/2, 18 – 8/3, 06	E80 STER-EO-B	8/1, ∼14
1	M	2			(M2) 8/2, 12:52			(M2) 8/3, 05:54			M2 8/4, 02:50				SM1 8/3, 20 8/2, 18 – 8/4, 12	E30 VEX-L_1	8/2, ∼02 8/3, 23 (T–H)
2	L	–	S2 8/2, 11:30	–	M3 8/2, 19:51	S2 8/3, 05:00		M3 8/3, 21:50	S2 8/3, 17:05			S2 8/2, 09:43			SM2 + SM3 8/3, 12 – 8/5, 00	0 L_1	8/3, ∼18 8/4, 03 (T–H)
3	A?	3								Y 8/4, 07:18	M3 8/4, 09:38		–	? 8/2, 21:34	SM2 8/4, 02	0 L_1	
4	B	–								Y 8/4, 09:44			–	? 8/3, 12:14	SM3 8/4, 16	0 L_1	
5															SM4 8/6, 00	W22 L_1-ST-A	8/5, ∼20 8/6, 11 (T–H)

Notes: Source Long. = SEL means the ecliptic longitude relative to the Sun–Earth line. The activity type is taken from the SDO observations except for CME0, which was observed as a halo CME at STEREO-B. – = Not studied or not measured. ? = Unknown or uncertain. H = Harrison *et al.* (2012). L = Liu *et al.* (2012). CMEs 0 – 4 are same as in Odstrcil *et al.* (2013). * = Shock and magnetic feature designations and timings from Möstl *et al.* (2012). T–H = Tappin–Howard model reconstruction (see Section 4.2).

J-track designation from Harrison *et al.* (2012) and Liu *et al.* (2012) and the range of onset times derived by Harrison *et al.* (2012); Column 6 the approximate source Earth-facing longitude and main type of activity; Column 7 the ecliptic trajectory longitude derived from J-tracks by Harrison *et al.* (2012) or Liu *et al.* (2012); Column 8 the name of the spacecraft or planet that may have been impacted by the CME flow or observed by SMEI; Column 9 the range of 1 AU arrival times from the Harrison *et al.* (2012) J-maps; and Column 10 the *in situ* times of possibly associated density enhancements at the designated 1 AU locations.

Linked by the same CME number designations, Table 1b gives our interpretations of the associations, timings, and trajectories of the *in situ* signatures of the CMEs observed at four spacecraft. These include the shocks and magnetic flux ropes (MFRs) as described by Möstl *et al.* and Liu *et al.* (see below) and density enhancements as determined by us, as observed by VEX at Venus, STEREO-B, *Wind* at L_1 and MESSENGER. VEX and MESSENGER obtained no useful plasma data and, hence, have no suitable density measurements available. In the last three columns we list for each density structure, designated by 'SM#', as determined from the SMEI 3D reconstructions as discussed in Section 4, i) the time of the SMEI density peak and the range of enhanced density there, ii) the approximate ecliptic longitude direction and spacecraft location of the density structure, and iii) the approximate arrival time at 1 AU of the density front.

3.2. Summary of *in situ* Analyses of the CMEs

Our goal in this paper is to use heliospheric imaging observations and density reconstructions to connect the CME, HI tracking, and *in situ* analyses to understand the general nature of these events. In this subsection we discuss the context of the *in situ* measurements and flux-rope modelling.

Figure 1 presents an overview of the spacecraft positions in heliocentric Earth-ecliptic (HEE) coordinates on 1 August 2010. Figure 5, from Möstl *et al.* (2012), is a stackplot of the total magnetic field strengths at the five spacecraft ordered from top to bottom of their longitudes from east to west of the Earth. Möstl *et al.* (2012) identified two shocks, S1 and S2, in these *in situ* data sets, with S1 detected only at the eastern locations of VEX and STEREO-B and S2 detected at all but the STEREO-A spacecraft locations, spanning 120°. Möstl *et al.* (2012) also identified a set of three distinctive, consecutive magnetic features, called M1, M2, and M3, at the STEREO-B, VEX and L_1/*Wind* spacecraft. For example, the M1 and M2 structures appeared first at VEX, then later and farther out at STEREO-B, and even later at *Wind*. Figure 5 shows that the overall total magnetic field, B, profile observed by VEX is qualitatively similar to that at STEREO-B, which were separated by 18° in longitude, while the B profile looks quite different at *Wind* and MESSENGER, each successively farther to the west. An enhanced magnetic field following the S2 shock was observed at MESSENGER and was modelled as a brief flux rope (M1) by Möstl *et al.* (2012) with its axis close to the ecliptic. There were no shocks or other distinctive magnetic features at STEREO-A, and, as noted above, there were no transient signatures there during this entire period, only an HSS (Figure 3). Thus, the STEREO-A *in situ* data provide a definitive western boundary, which shows that the multiple sequence of events did not extend into the ecliptic heliosphere that far westward at the 1 AU distance.

From its trajectory and velocity shock, S1 was very likely associated with M1, at least at VEX and STEREO-B. Its source was probably CME 0, observed to the solar northeast on 30 July by COR2-A and as a halo CME by COR2-B (also see Liu *et al.*, 2012; Möstl *et al.*,

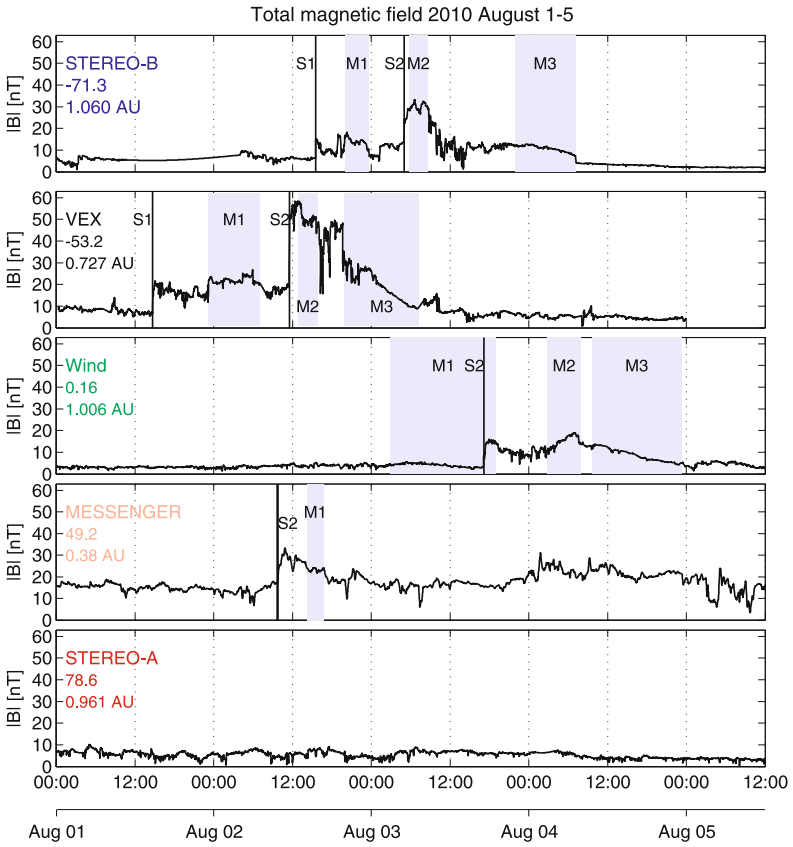

Figure 5 The total solar wind magnetic field observed *in situ* at five well-separated locations in the inner heliosphere (≤ 1 AU) close to the ecliptic plane. From east (STEREO-B) to west (STEREO-A) the spread in heliospheric longitude is 149.8°, and the CMEs are observed *in situ* from STEREO-B to MESSENGER, corresponding to 120.5° in longitude. From top to bottom (or east to west): the total magnetic field at STEREO-B, VEX, *Wind*, MESSENGER, and STEREO-A. Vertical solid lines indicate shock arrival times. Shaded intervals indicate well-observed magnetic flux-rope-like structures. Adapted from Möstl *et al.* (2012), their Figure 1b.

2012 and Odstrcil *et al.*, 2013). M1 was a fairly weak magnetic structure at STEREO-B, VEX, and *Wind*, and was not clearly a magnetic cloud, as determined by its rotational or plasma characteristics (*e.g.*, Burlaga *et al.*, 1981). However, Liu *et al.* (2012) determined that this was an *in situ* CME (their #1) at STEREO-B and *Wind* based on its low plasma β and magnetic rotation signatures (*e.g.*, Zurbuchen and Richardson, 2006). On the other hand, we will see below from the heliospheric density modelling that the M1/CME1 structures at VEX and STEREO-B versus at *Wind* might have come from different CME flows.

Temmer *et al.* (2012) and Liu *et al.* (2012) suggested that the more extensive shock S2 resulted from the merger of CMEs 1 and 2 (Liu's 2 and 3 – see Table 1a), which are identified with the HI-A J-tracks, M and L (Harrison *et al.*, 2012). As discussed in Section 4.3, Odstrcil *et al.*'s (2013) ENLIL simulations suggest that the combined CMEs 1 + 2 would mainly have impacted VEX and STEREO-B but its western flank might have brushed L_1/Earth (see Figure 12).

Möstl *et al.* (2012) noted that at *Wind* the M2 and M3 structures followed S2 and its apparent shock sheath (Figure 4). These structures have been successfully modelled as flux ropes using the Grad–Shafranov (G–S) reconstruction technique (Hu and Sonnerup, 2002; Hu *et al.*, 2004; Möstl *et al.*, 2009a, 2009b). The related M2 and M3 structures at VEX and STEREO-B were fit as flux ropes by the G–S, minimum variance, and/or force-free techniques. M3 was longer-lived than M2, but had lower total flux, and more clearly fit the definition of a magnetic cloud (Burlaga *et al.*, 1981). It was left-handed and highly inclined to the ecliptic plane. However, the fits to M3 at both VEX and STEREO-B were similar to each other but different from that at *Wind*. The VEX and STEREO-B M3 flux ropes were right-handed and quasi-parallel to the ecliptic. Möstl *et al.* (2012) interpreted these fits as being consistent with a single flux rope structure that is slightly bent along its axis between the two spacecraft. STEREO-B appeared to pass near the apex of the structure, whereas VEX may have passed through its western leg. The M3 flux rope at *Wind* was most likely not the same structure and may not have had the same source-CME.

The results of Möstl *et al.*'s (2012) fits to the *Wind* data that are the most relevant to this paper are the following: The onset of M2 was on 4 August, 04:34 UT and extended until the leading edge of M3 arrived at 4 August, 10:07 UT. Both MFRs were associated with low-variance magnetic field and smooth rotation of the magnetic field direction. M3 appeared to be expanding radially when it passed *Wind*. In contrast, M2 was not expanding, presumably because of compression by M3. Liu *et al.* also noted that these CMEs were in the process of merging and that "CME1" (M2) was being "significantly compressed, accelerated and heated by the overtaking shock" (S2). These authors also suggested that the region between their CMEs 1 and 2 had enhanced density, temperature, and β, possibly because it was the interface of their interaction. The enhanced density on 4 August at around 06:10 UT, peaks labelled 'D1' and 'D2' in Figure 4, is of particular interest here and is discussed below. M2 was inclined slightly to the ecliptic and pointing northward, and M3 was more inclined and pointing southward at almost $-45°$. The two M2 and M3 axial fields pointed approximately toward solar west.

Flux-Rope Fit Modelling We performed a suite of analyses of two sets of the *in situ* CME events that occurred in August 2010 as observed by the VEX, STEREO-B, and ACE spacecraft (ACE and *Wind* were both in orbit about the L_1 position and had similar solar wind data). The analyses included force-free flux-rope modelling and multipoint *in situ*, non-force-free, flux-rope modelling using the Mulligan (2002) method. For consistency we used the earlier Möstl *et al.* (2012) nomenclature for each CME in the series. These correspond to M2 at VEX and STEREO-B and M2 at *Wind*/ACE, and M3 at VEX and STEREO-B and M3 at *Wind*/ACE (see Figure 5). However, our event boundaries differ slightly from those of Möstl *et al.*, because in the G–S method the boundaries are determined by the technique. Our boundary choices were driven by the magnetic field and plasma signatures, and the arrival timing of the events did not take account of the similarity of the field rotation at each spacecraft.

An initial orientation analysis was performed on the left-handed M2 structure at VEX and STEREO-B using static, force-free, flux-rope modelling of magnetic cloud structures as introduced by Burlaga (1988). This gives the orientation of the flux ropes and the impact parameter (the closest distance the spacecraft passes from the tube's axis). The magnetic field configuration at these spacecraft was magnetic cloud-like, including non-significant expansion within the crossing time, enabling straightforward difference-minimisation fitting to a unique (non-degenerate) solution. The fit results are listed in Table 2a. The structure of M2 at ACE was not force-free, and the point in time at which the structure began its passage was not clear.

Table 2 (a) Results of static, force-free modelling of the left-handed flux rope, M2 Structure at STEREO-B and VEX. (b) Results of flux rope modelling of M3 structures at STEREO-B, VEX and ACE (L_1).

(a)

Spacecraft	Lat.	Longitude (0 = Sun–object line)	Impact Parameter (% of flux rope radius)	Magnetic field strength (at centre of flux rope)
STEREO-B	−54°	−69°	∼0	31 nT
VEX	−66°	37°	40 (−y side)	51 nT

(b)

s/c (flux rope)	STEREO-B (M3)	VEX (M3)	ACE (M3)
handedness	right-handed	right-handed	left-handed
orientation [lat, lon[a]]	[3.4°, 137°]	[−17.1°, 141°]	[−78.4°, −149°]
B field signature	NES	unclear	WSE
s/c traversal	near apex crossing	leg crossing	apex crossing
radial size	0.140 AU	0.145 AU	0.097 AU
B flux lower bound	12.6×10^{21} Mx	12.1×10^{21} Mx	5.6×10^{21} Mx

[a]Longitude defined in solar ecliptic coordinates ecliptic plane; 0° along s/c–Sun line. Positive angle toward the $-y$ axis (opposite planetary motion) or counter-clockwise as viewed from the $+z$ axis.

Möstl *et al.* (2012) concluded that the M2 structure at VEX and STEREO-B was probably just the shocked part of the M1 structure and not a separate CME/flux rope. Our results here do demonstrate that the M2 structure can be successfully modelled as a flux rope at both spacecraft. However, the ambient magnetic field can be compressed and drape around an CME structure as it transits through slower solar wind, resulting in a field with an *in situ* rotational magnetic signature that is not necessarily a flux rope. Therefore, we cannot conclude whether the M2 structure was a flux rope and will not discuss it further.

In contrast, the M3 structures at STEREO-B, ACE, and *Wind* met all standard criteria for magnetic clouds, and the magnetic signatures at VEX suggest a flux rope, but the lack of plasma data prevents us from confirming it as a magnetic cloud. For M3, we find the flux rope fits at VEX and STEREO-B resulted in right-handed structures while the ACE fit showed another structure with the opposite sign. In addition to the different sign and orientation, the ACE rope had a much smaller radial size and contained far less magnetic flux than the ropes at STEREO-B and VEX. It is also clear that VEX passed through the structure along the western leg. These parameters are all consistent with STEREO-B and VEX observing a single flux-rope structure that was slightly bent along its axis between the two spacecraft. The differences in these same parameters at ACE indicate that the flux rope observed at ACE was most likely a different structure than that observed at VEX and STEREO-B. In general, our results confirm those of Möstl *et al.* (2012) for these M3 structures even though these authors used different techniques for fitting M3, *i.e.*, minimum variance at STEREO-B/VEX and G–S at *Wind*. Table 2b provides a summary of our modelled flux-rope (M3) parameters.

Figure 6 shows the chosen flux rope boundaries and fits to the magnetic structures M3 at VEX and STEREO-B and M3 at L_1/ACE. The resulting flux rope orientations are illustrated in Figure 7 and show two 3D views ("can" diagrams) of the flux ropes at VEX, STEREO-B, and ACE, with the Earth orbit shown as a green ellipse. Dipole field lines thread all three

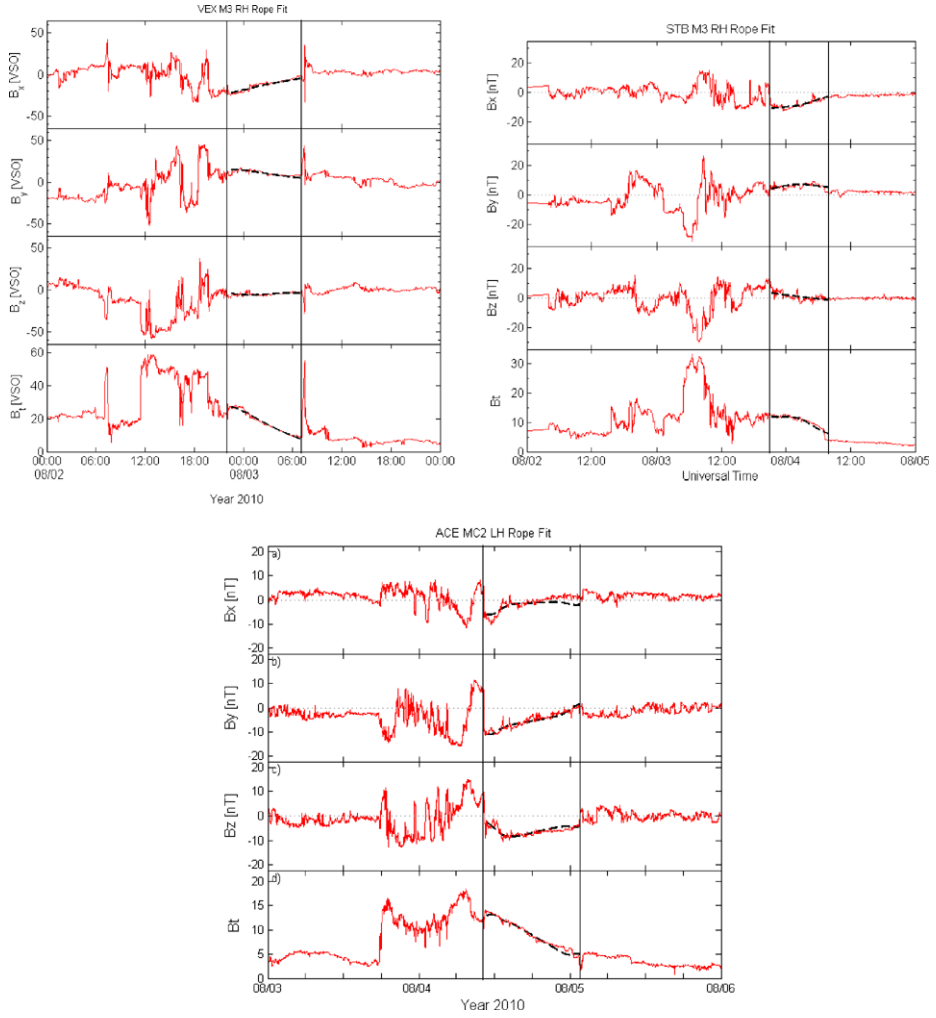

Figure 6 Cylindrical flux-rope fits to Möstl *et al.* (2012) magnetic structures M3 at VEX and STEREO-B and M3 at L_1/ACE. (a) The VEX magnetic field data during "M3" and the flux-rope fit are shown in the local VSO coordinate system: x points radially toward Sun from Venus, z points northward, and y is opposite the planetary motion (analogous to GSE if VEX were located at the Earth). Note the VEX magnetic field rotations are similar to STEREO-B. (b) STEREO-B magnetic field data during "M3" and flux-rope fit shown in local coordinate system: x points radially toward the Sun, z points northward, and y completes the right-hand coordinate system (analogous to GSE if STEREO-B were located at the Earth). (c) ACE magnetic field data during "M3" and flux rope fit shown in local GSE coordinates. Note the flux-rope magnetic field rotations are different than at VEX and STEREO-B, especially By, which is in the opposite sense than those at STEREO-B and VEX. In all three plots the flux-rope boundary is delineated by the vertical lines.

cans to aid visualisation of the rope orientations, and the axial field directions are indicated by black arrows (compare with Figure 8 from Möstl *et al.*, 2012). Determination of the M3 CME speed at VEX is possible using the difference of M3 arrival times between VEX and STEREO-B assuming that the CME propagated outward from VEX to STEREO-B and was halfway between them. These fits reflect the radial sizes of the ropes as determined by using the averages of the leading and trailing edge *in situ* speeds at all three locations:

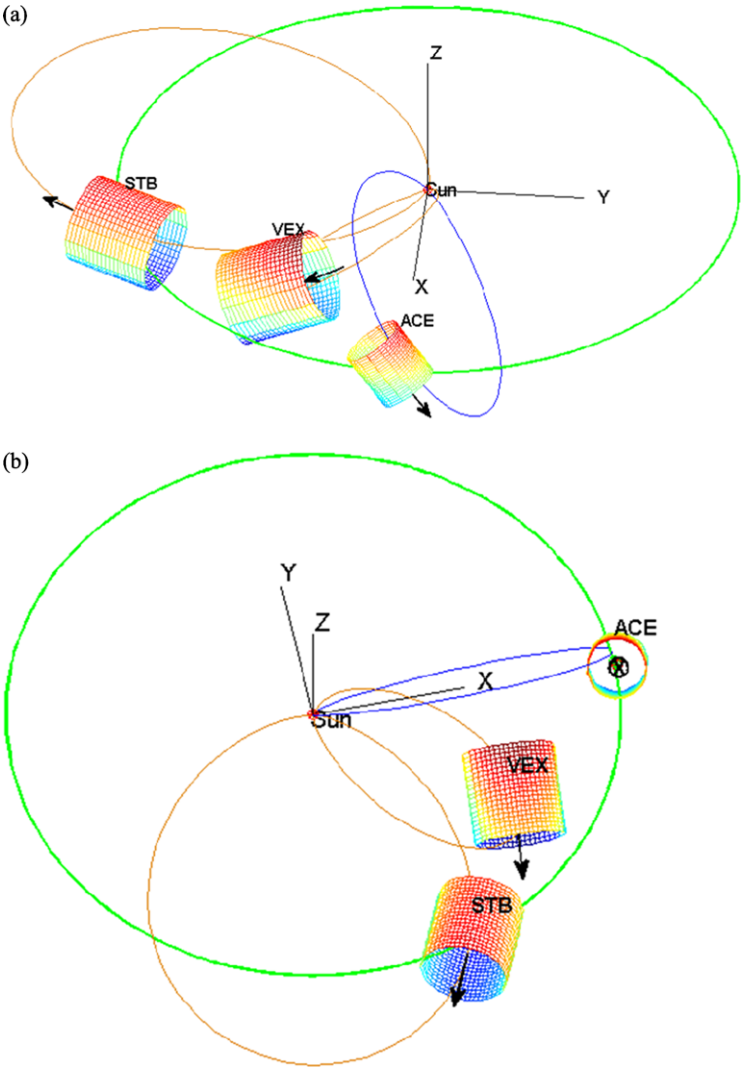

Figure 7 Two different 3D views of the VEX, STEREO-B, and ACE flux-rope fits in a Sun–Earth coordinate system. The Earth orbit is shown as the green ellipse. Dipole field lines thread all three cans to aid visualisation of the rope orientations. Axial-field directions are indicated by the black arrows. The VEX and STEREO-B flux-rope fits are right-handed and oriented quasi-parallel to the ecliptic plane, whereas the ACE flux rope is left-handed and is quasi-perpendicular to the ecliptic plane. The VEX and STEREO-B fits are consistent with a single flux-rope structure that is slightly bent along its axis, while the ACE fit is inconsistent with those at VEX and STEREO-B and is possibly another structure.

VEX = 598 km s^{-1}, STEREO-B = 586 km s^{-1}, and ACE = 525 km s^{-1}. The flux rope at VEX has a radial size of nearly 0.145 AU and at STEREO-B is similar, 0.140 AU. The magnetic flux approximations within the ropes at VEX and at STEREO-B are similar at 12.1×10^{21} Mx and 12.6×10^{21} Mx, respectively. These fluxes are consistent, but represent a lower bound to the magnetic flux due to the expected oblate cross-section of the ropes. The radial size at ACE is 0.097 AU and the lower bound magnetic flux is $\sim 5.6 \times 10^{21}$ Mx.

4. Heliospheric Imaging: 3D Density Reconstructions and MHD Simulations

4.1. UCSD SMEI Density Reconstructions

The analysis of the white-light heliospheric images from SMEI employed here follows the UCSD 3D computer-assisted tomography analysis chain as developed and used by, *e.g.*, Jackson *et al.* (2006, 2010a, 2010b, 2011) and Bisi *et al.* (2008). The UCSD technique determines the 3D extent of heliospheric structures by using the line-of-sight response in Thomson-scattered light, and iteratively fitting these from limited viewing locations. For observations covering a wide range of solar elongations, heliospheric structures are seen from widely different perspectives as they move past the Earth, allowing time-dependent 3D reconstruction of transient structures. At present, the reconstruction incorporates a purely kinematic solar wind model. Given the velocity and density on an inner boundary (the "source surface"), a fully 3D solar wind model is derived by assuming radial outflow and enforcing conservation of mass and mass flux. If the 3D solar wind model does not match the overall observations, the source surface values are altered to minimise the deviations and achieve a best fit.

The SMEI UCSD group has produced 3D reconstructions of the heliospheric density observed by SMEI during this period. The images have a spatial resolution of 3.3° and a temporal resolution of 0.25 days, an improvement of about a factor of two over previous UCSD reconstructions. Without other knowledge of velocities in the inner heliosphere, a constant velocity of 650 km s^{-1} was assumed for this SMEI density reconstruction. This velocity was similar to the *in situ* transient velocities and yielded the best comparisons in reconstruction timings of the events at each of the *in situ* points of comparison (see below). The online SMEI reconstruction movies show these images over the period of 1 – 7 August, both in the plane of the ecliptic and in meridional planes through the ecliptic north and south poles spaced at 3° intervals in longitude.

Figure 8 shows an example of the 3D reconstruction on 4 August, 00 UT showing the density flows in the ecliptic plane viewed from the north; the large circle is the Earth orbit and the small circles denote the locations of the Earth (E), the STEREO spacecraft (A, B), Venus (V), and MESSENGER (M). The dense material in the SMEI meridional view (Figure 8) just arriving near Earth on 4 August, 00 UT, is very likely material from the extended SM2 and SM3 (ecliptic plane) structures (Figure 9) that overlap in longitude along the line of sight. Thus, the meridional view probably integrates material from all three of the CMEs tracked in HI-A, which we call CMEs 2, 3, and 4. The material extending to the north is probably associated with CME 3, the northernmost CME–filament eruption, which is also the northernmost CME observed in the coronagraph and HI-1 (CME A) images. There are prolonged flows extending just north of the ecliptic back toward the Sun. (Again, we note that the dense structure south of the ecliptic may be noise in the images and do not consider it further.)

Figure 8 shows our identification of five possible heliospheric CMEs in the ecliptic from the same frame of the high-resolution SMEI movie on 4 August, 00 UT. The centroids of the peak densities within the most significant flow structures during this period are marked with arrows and labelled with the "SM#" nomenclature in the last three columns (SMEI) of Table 1b. We considered a density structure to be "significant" if it had a core density $> \sim 20$ cm^{-3}, exhibited a coherent, radial motion during the movie sequence, and eventually moved past 1 AU. The CMEs are labelled SM0 (for "SMEI" CME 0) to SM4 to suggest these matches of the heliospheric flows with the six CMEs, CME 0 to CME 5, in Table 1b. We describe these flows from east to west of the Sun–Earth line, or from bottom to top in the figure.

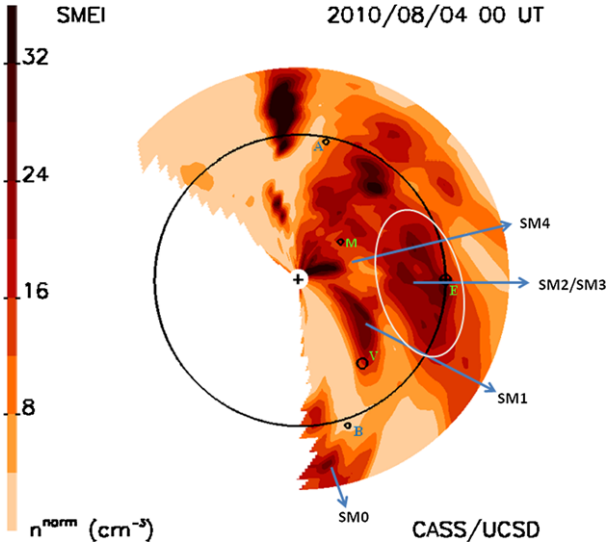

Figure 8 Snapshot of the SMEI 3D density reconstruction on 4 August, 00 UT from the CASS UCSD imaging group. These are from the online movies that show these flows from 1 – 7 August. This is an ecliptic-plane view of the reconstruction with the locations of STEREO-A, the Earth, MESSENGER, Venus, and STEREO -B marked with small circles and letters. The scale denotes increasing density as being darker. The peak density centres of the most significant flow structures are located with the arrows and labelled with the "SM#" nomenclature in Table 1b, SMEI columns. The white oval outlines the extended region of enhanced density that contains SM2 and SM3. Notable are the double-density peak in the Earth-directed flow, and the flows along the Sun-STEREO-B line, between STEREO-B and the Earth, and between the Earth and STEREO-A.

SM0 was associated with CME 0, on 30 July, observed as a halo from STEREO-B. The main SMEI flow was extended over a day and a half and moved radially east of STEREO-B. Figure 9(b) shows the profile of the SMEI-reconstructed flow past the STEREO-B location compared with the smoothed STEREO-B density. The SMEI flow there lasted from 2 August, 18 UT, to 4 August, 06 UT, with a peak on 3 August at 06 UT. This agrees well with the time of the two shocks and the M1 and M2 magnetic regions but slightly lags the peak and region of enhanced density at STEREO-B. As stated above, the UCSD reconstruction depends on a kinematic solar wind model with a fixed, constant speed. We ran the model with two wind speeds, an average of 400 km s^{-1} wind and a higher speed of 650 km s^{-1}. This faster speed is consistent with the wind speed behind shock S2 at both STEREO-B ($\sim$650 km s^{-1}) and wind ($\sim$575 km s^{-1}), which was much faster than in front of it (Figures 9 and 4).

SM1 is associated with either or both CME 1 and 2. The SMEI flow past Venus lasted nearly two days. Figure 9(a) shows the profile of the SMEI-reconstructed flow past the VEX location, lasting from 2 August, 18 UT, to 4 August, 12 UT, with a peak on 3 August at 20 UT. Although there were no plasma data at VEX, this time range matches the strong trailing magnetic regions M2 and M3 in Figure 5. Figure 8 shows that the core of SM1 lay west of VEX and some 30 – 40° east of the Sun–Earth line. This is the trajectory predicted for CME 2 (see the source latitudes and longitudes in Odstrcil *et al.*'s (2013), Tables 1 and 2), although CME 1 would also have gone to the east. Since most analyses conclude that CMEs 1 and 2 began to merge near the Sun, SM1 could be the massive core of the merged region that was slowed during its passage (its core did not reach 1 AU until 5 August).

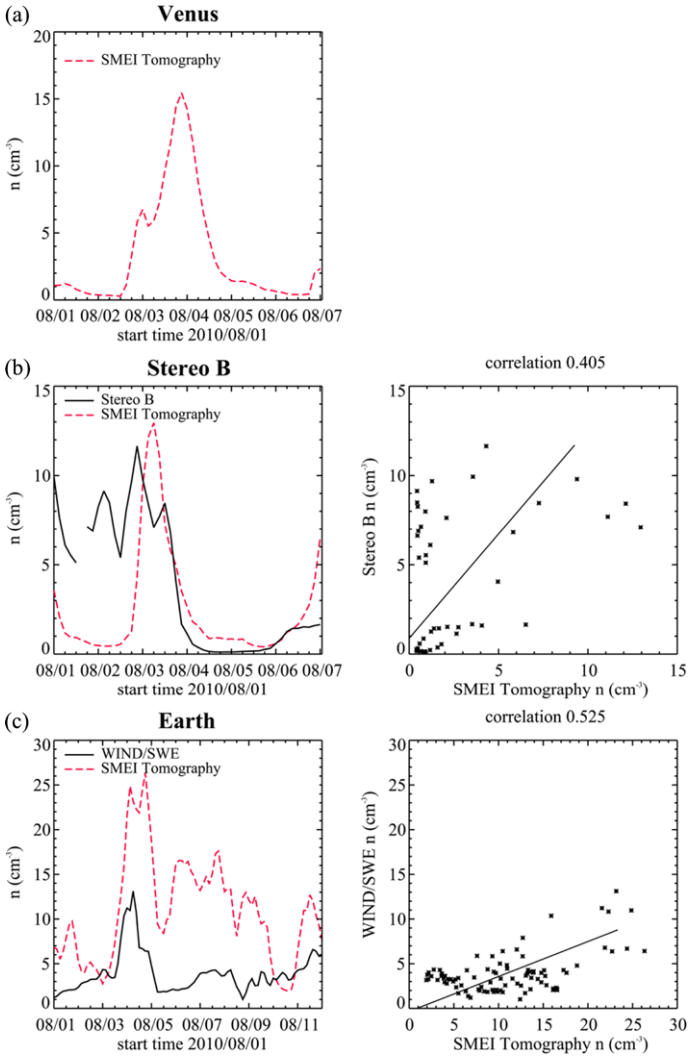

Figure 9 The SMEI-reconstructed densities at the locations of (a) Venus and (b) STEREO-B from 1 – 7 August and at (c) *Wind* from 1 – 11 August. At Venus the peak values in late 2 August – early 3 August are generally consistent with the timing of the enhanced total magnetic field flux at VEX (see Figure 5). The SMEI reconstruction assumes a constant speed of 650 km s^{-1}, equivalent to the high speeds following the S2 shock at both STEREO-B and *Wind*. At STEREO-B and *Wind* the SMEI-reconstructed and *in situ* STEREO-B PLASTIC and *Wind* SWE densities are compared. Similar results were found using the SOHO CELIAS and ACE instruments (not shown). The spacecraft densities have been averaged with a 0.65-day boxcar average. The SMEI results use the higher 3D resolution of 3.3° in latitude and longitude and a 0.25-day temporal resolution. Note that the double peak in the SMEI data late on 3 August and midday on 4 August occurred during the enhanced density period on the *Wind* plot. The SMEI-STEREO-B and SMEI-*Wind* density plots have correlations of 0.405 and 0.525, respectively, which is reasonable considering they are averaged over $\geq$ 7 day intervals.

The SM2 and SM3 structures are the dense cores of a large band of enhanced density that extended over 50° in longitude from east to west of the Sun–Earth line (outlined by the

white oval). The dense cores SM2 and SM3 are approximately situated along the Sun–Earth axis (Figure 1). The enhanced SMEI-reconstructed density flow almost exactly matches the time of enhanced density *in situ* at *Wind* at L_1 (Figures 9 and 5). The general SMEI density enhancement there ranged from 3 August, 12 UT to 5 August, 00 UT. This time frame encompassed the shock (S2) sheath and regions M2 and M3. Given the relatively coarse temporal resolution, the SMEI double-density peaks at the L_1 location, on 4 August at $\sim$02 and $\sim$16 UT, seem consistent with the enhanced *Wind* density peaking at 07:18 (D1). Liu *et al.* (2012) concluded that the *Wind* enhancement was an *in situ* signature associated with the merger of two CMEs (our CMEs 1 and 2). In the previous section we noted that the M3 structure at L_1 was a clear magnetic cloud and modelled it (at ACE) as a high-inclination, left-handed flux rope. Thus, the SMEI density seems highest immediately in front of the flux rope. The identification of the SM2 and SM3 SMEI structures with the CMEs is less certain. We propose that this extended region might be associated with all or parts of CMEs 2, 3, and 4. In Table 1b we identify SM2 with CME 3 and SM3 with CME 4. However, since these form the western boundary of a dense structure extending east of the Earth, this extended structure could also be associated with CME 2, or the merged CMEs 1 and 2, as the ENLIL simulation shows (see below and Figure 12).

Temporally, the next coherent dense structure to cross 1 AU was a dense region directed well west ($\sim$55°) of the Earth, passing between the Earth and STEREO-A (Figure 8). A major portion of this region appeared as a planar structure in the ecliptic and is considered suspect for this reason because of the potential contamination in this region from lunar brightness. Southward and closer to the Earth near MESSENGER, this appears as a structure connected with the other structures that pass near the Earth.

Finally, SM4 was a large very dense structure that was located mostly west of the Sun–Earth line and was delayed with respect to the other structures. It arrived at 1 AU late 5 – early 6 August and its eastern edge might have brushed L_1/Earth. The SMEI-reconstructed density flow at the *Wind* location shows a second enhancement on 6 August, 00 UT that is not reflected in the *Wind* density profile (Figure 9). Thus, this feature must have missed L_1 to the west. This is confirmed by the Tappin–Howard modelling (see next section), which shows a structure that reaches 1 AU at this time and is centred 24° west of the Earth. We are not sure of the solar origins of this later feature detected by SMEI, but it could be related to the eruption of CME 5, the large southernmost filament eruption (Fil 3) late on 1 August.

4.2. Tappin–Howard SMEI and HI-A Density Reconstructions

In this section we present the results from a second kind of heliospheric image CME reconstruction tool. This technique, called the Tappin–Howard (T–H) model (Tappin and Howard, 2009a; Howard and Tappin, 2009), extracts basic 3D information about CMEs by comparing a dataset of simulated leading edges with the measured leading edges obtained across a sequence of many heliospheric images of a given CME. The model runs quickly and almost autonomously and therefore is well-suited to space-weather forecasting (Howard and Tappin, 2010). The CME front is modelled as a simple spherical arc centred on the Sun. Then independent combinations of speed, central latitude, central longitude, latitude width, and longitude width are combined to produce CME-simulated images from which leading edges are produced relative to a fixed observer. A distortion parameter is also a part of the calculation, which enables the concavity of the CME to change from that of a spherical shell. The model is run in two stages. Stage 1 converges to a solution that contains a unique combination of each of the six parameters. Along with a fixed direction and structure, this also produces a single speed, allowing only for a constant-speed CME estimate. Stage 2 uses

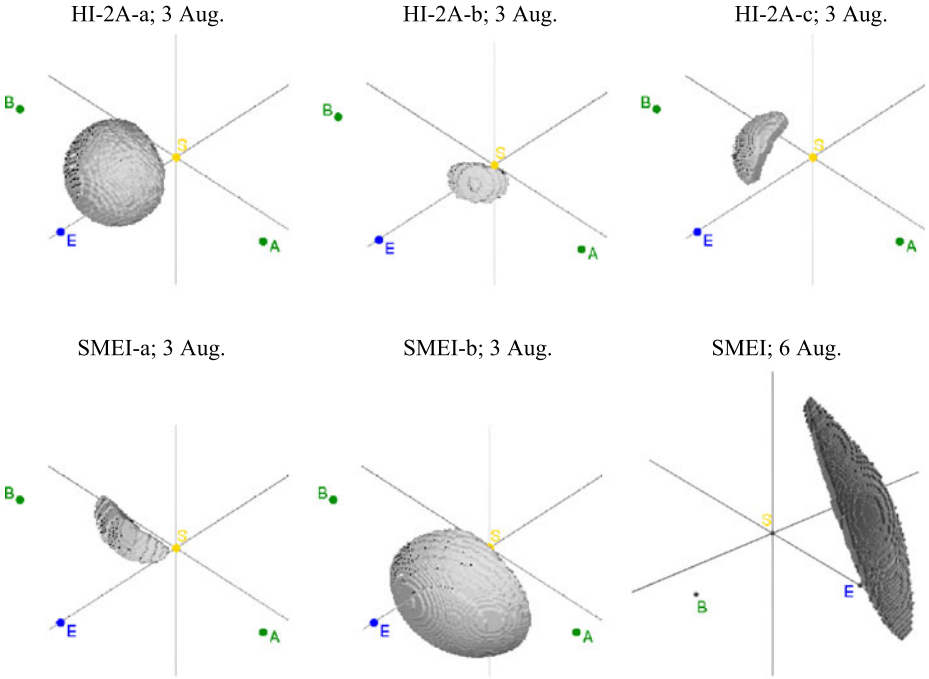

Figure 10 Tappin–Howard 3D reconstructions of separate density fronts observed with the HI-2A (top three panels) and SMEI (bottom panels, a and b) instruments on 2 – 3 August. These five views are taken all at the same time, 3 August 2010 at 01:50 UT, and as viewed from the same location relative to the ecliptic, N40°W45°. The locations of the Sun (S), the Earth (E), and STEREO (A) and (B) are indicated. Bottom right: T–H reconstruction of a CME observed by SMEI on 6 August at 10:08 UT, when the central part of the CME was at 0.9 AU. The view is from above the ecliptic at N30°E40°.

the results of Stage 1, but allows selected parameters, usually the speed, to vary to estimate their evolution.

Figure 10 shows 3D reconstructions of the August 2010 events from T–H fits using leading-edge measurements from the HI-2A (top) and SMEI (bottom) data. These are 3D isosurfaces of the leading-edge densities as derived from the model. The first five panels show the reconstructions at the same time, on 3 August 2010 at 01:50 UT, and as viewed from the same location north and west of the ecliptic. The bottom right panel shows the reconstruction of another later event west of the Earth that reached 1 AU on 6 August (discussed below). The T–H best-fit parameter results for each event are listed in Table 3.

In Table 3 Lat and Long are the central latitude and longitude in degrees of each CME in heliocentric-ecliptic coordinates. DLat and DLon are the latitude and longitude angle from the CME centre to the edge, *i.e.*, the latitude and longitude half width. For the spherical arc geometry case a distortion factor D is used that governs the distortion of the spherical structure of the bent shell. The surface is determined by the relation

$$\varphi = \cos^{-1}\left(r'/r\right)D$$

where r is the distance from the Sun to the leading edge of the structure along the central axis of the CME and r' is the distance from the central axis to the surface of the bubble at an angle, ψ, to the axis (see Howard and Tappin, 2010). Values of D vary from 0 being

Table 3 Geometric results from the T–H model for the August 2010 events.

CMEs	Lat (°)	DLat (°)	Long (°)	DLon (°)	Distortion
3 August					
SMEI-a	36.2N	11.1	7.4E	36.0	−0.41
SMEI-b	*5.5S*	*53.4*	*21.8W*	*45.6*	*0.20*
HI-2A-a	*11.1N*	*42.0*	*11.0W*	*43.7*	*1.16*
HI-2A-b	27.9N	12.0	32.2W	20.0	1.28
HI-2A-c	32.1N	32.6	15.5E	13.0	0.83
6 August					
SMEI	24N	106	24W	40	−0.63

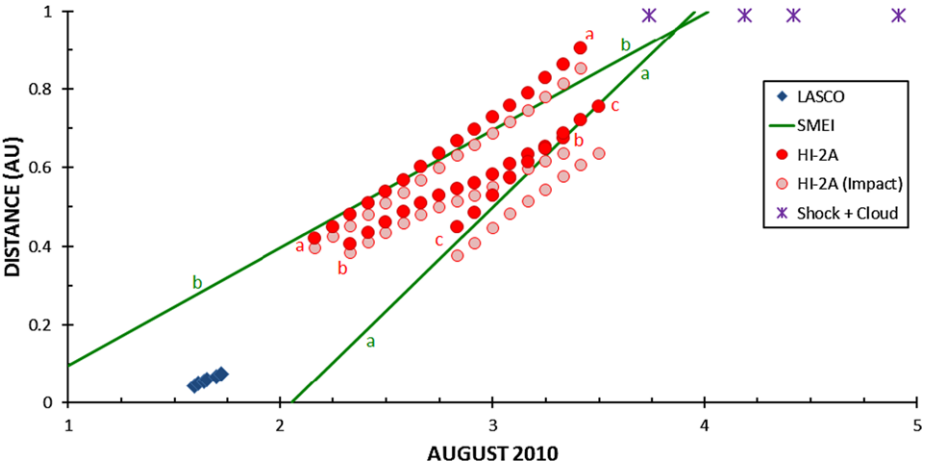

Figure 11 Distance–time plots derived from T–H fits for HI-2A and SMEI data. Red denotes the nose of the CME from HI-2A data; pink shows the earthward-directed part of the same CME (HI-2A); and green denotes constant speed trajectories of the CMEs from SMEI data alone.

a simple shell, $D > 0$ a more curved shell, $D = 1$ approximating a spherical bubble, and $D < 0$ being less curved than a simple shell.

Figure 11 is the distance *vs.* time (d–t) plot that results from the T–H runs for the 1 – 3 August CMEs shown in Table 3. The Y-axis is the heliospheric distance in AU that T–H reconstructs from the SMEI and HI data for each CME. The X-axis is the day in August 2010. The instruments used for the input data on each CME are labelled in the legend. There are two plots for each HI-2A event: Red is for the centre of the CME and pink is for the part of the CME that intersects (or most closely approaches) the Earth. We were unable to produce Stage 2 T–H results for the two SMEI events because there are not enough leading-edge measurements to provide convergence. Instead, the green lines are for the Stage 1 results, which produce constant-speed trajectories of the SMEI events, yielding speeds of SMEI-a = 913 km s^{-1} and SMEI-b = 520 km s^{-1}. We were able to produce Stage 2 results for the HI-2A CMEs, which are shown as individual data points.

Because the T–H model produces a 3D reconstruction of the CME front, the arrival time at, or closest approach to, any heliospheric object such as a planet or spacecraft can be estimated as well as the "miss angle" between the central axis or edge of the structure and

the object of interest, and we can calculate the probability for the CME to impact the object (Howard and Tappin, 2010). For the August events these parameters are given in Table 4. The table can also be used to indicate the approximate arrival times at 1 AU of the reconstructed features.

Taking these results at face value, one interpretation that appears consistent with the geometry, trajectory, and *d–t* results is that the HI-2A-a and SMEI-b density fronts (italicised in Tables 3 and 4) are likely the same physical feature. This feature would have impacted the Earth, arriving late on 3 August or early on 4 August. This feature is most consistent with the merged tracks M and L, ENLIL CMEs 1 + 2 and the UCSD SMEI features SM2, SM3 (and/or possibly part of SM1). The arrival time of the SMEI-b feature is associated with SM2 and SM3 in Table 1b, and given in the last column (the arrival times in brackets in Table 4 are considered very unlikely due to their low impact probabilities and were therefore not used). The arrival times from these two independent reconstructions of the SMEI data are consistent to within several hours. The exact timing of these density features with the *Wind in situ* density peaks is unclear, however, since the *Wind* density was enhanced from late 3 August through 4 August.

The smaller HI-2A-c and SMEI-a fronts look similar, although with a different rotation, and are close in time and location, so may be the same feature. This feature appears to have a trajectory between STEREO-B and the Earth. The fast speed, 913 km s^{-1}, of the T–H SMEI-a CME is consistent with CME 2, which was the fastest of this series of CMEs. Harrison *et al.* (2012) and Liu *et al.* (2012) derived a range of speeds for CME 2 (L) from 700 – 1100 km s^{-1}; the T–H speed is in the centre of this range. This is the location of the UCSD SMEI SM1 feature, and it may have missed both STEREO-B and the Earth. The arrival time of the SMEI-a feature is associated with SM1 in Table 1b and listed in the last column. Thus, the arrival times at 1 AU derived from the independent UCSD and T–H reconstructions are consistent with each other to within a few hours.

Besides these density fronts on 2 – 3 August, there was the later event west of Earth that reached 1 AU on 6 August. Figure 10 (bottom right panel) shows the T–H fit of this CME observed by SMEI and arriving at 1 AU on 6 August. The UCSD reconstruction (Figure 8) shows it to be a broad structure (SM4) that lies between the Earth and STEREO-A and just grazes the Earth. The T–H reconstruction is shown on 6 August at 10:08 UT, when the central part of the CME was at 0.9 AU. The view is from above the ecliptic at N30° E40°. The arrival time of the 6 August SMEI feature is listed in Table 1b, last column and, as with the above features, the arrival times from the independent reconstructions are consistent to within several hours.

Again, no T–H Stage 2 results could be obtained for the 6 August SMEI CME, hence we could not plot *d–t*. The results from Stage 1 give a speed of 985 km s^{-1}. The structure was too far from STEREO-B to have an effect there. Thus, the results suggest this was a fast CME directed somewhat north and west of, but probably grazing, the Earth and missing STEREO-A, and more extended in latitude than longitude. These results are consistent with the UCSD reconstruction, which shows a density enhancement near the Earth on 6 August (Figure 9) and no CME signature at STEREO-A. The source of this event is unclear.

4.3. Comparison with the Odstrcil *et al.* (2013) ENLIL Simulations

Numerical modelling and simulations can play an important role in clarifying the connection between solar transients and their effects in the heliosphere, provide a general context and suggest what may and/or what may not be observed. Since the origins of CMEs are still being studied so that real events cannot yet be routinely simulated end-to-end, Odstrcil

Table 4 Space-weather results from Tappin–Howard density reconstructions.

Event	Miss angle (°)			Impact probability (%)			Predicted arrival or time of closest approach Day, UT of August 2010		
	Earth	STEREO-A	STEREO-B	Earth	STEREO-A	STEREO-B	Earth	STEREO-A	STEREO-B
SMEI a	26	70	53	35	0	0	3, 23:09	(3, 20:15)	(4, 00:47)
SMEI b	*Impact*	*11*	*48*	*75*	*60*	5	*4, 02:59*	*4, 04:40*	*(4, 13:24)*
HI2A a	*Impact*	*46*	*18*	*75*	5	*45*	*3, 21:00*	*(5, 13:11)*	*6, 00:19*
HI2A b	27	37	85	35	10	0	4, 18:04	(4, 13:43)	(4, 23:51)
HI2A c	3	61	29	65	0	33	4, 10:30	(4, 07:13)	4, 13:17
SMEI August 6	4	29	65	65	40	0	6, 11:15	6, 09:12	(6, 13:06)

and colleagues have developed an intermediate "hybrid" modelling system that combines empirical, analytical, and numerical MHD models.

Odstrcil *et al.* (2013) use this hybrid ENLIL code to reconstruct the general heliospheric scenario during the early August 2010 period and show the appearance of the CMEs as temporal profiles and synthetic white-light images. This enables direct comparisons with *in situ* measurements and remote-sensing observations, such as first performed by Odstrcil, Pizzo, and Arge (2005) and presented in this paper. This 3D MHD numerical code uses two types of input at its inner heliospheric boundary (21.5 R_s). The background state is driven by WSA maps for 1 August that were used for the whole computational period under the assumptions of corotation and minimal changes. The CMEs are added with two different sets of the fitted geometric and kinematic parameters derived from coronagraph observations: i) using the geometric localisation technique (*e.g.*, Pizzo and Biesecker, 2004; de de Koning, Pizzo, and Biesecker, 2009) and ii) an erupting flux-rope model (Krall and St. Cyr, 2006; Xie *et al.*, 2009) technique. We refer to the Odstrcil *et al.* (2013) paper for more details. Here we show only two sets of resulting simulations from their paper that show the CMEs as 3D global structures, and their temporal profiles and synthetic white-light images. Figure 12 (their Figure 10) shows the simulated density between 0.1 and 1.1 AU in the ecliptic as viewed from ecliptic north for two different input cases and at three times on 1 – 2 August.

One can see from Table 1a, and Harrison *et al.*'s (2012) results, that the first three CMEs were launched with their axes east of the Sun–Earth line. This is also replicated in the ENLIL simulations, which show CMEs 0 – 2 travelling mostly to the east of the Earth. Likewise, CMEs 3 and 4 originated just west of the Sun–Earth line and, although weak and narrow, ENLIL shows them to be aimed mostly west. ENLIL also suggests that CMEs 1 and 2 merged and 3 and 4 merged, at least in their Case 1A (left side), with the faster 1 + 2 system driving a shock ahead (S2 in Figures 4 and 5). This interaction and shock are discussed by Liu *et al.* (2012) and Temmer *et al.* (2012).

Figure 12 shows the 30 July CME 0 as very extended in longitude and reaching 1 AU late on 2 August. The SMEI observations shown on 4 August in Figure 8 and in the online movie suggest that this is the feature SM0, and its time of arrival at STEREO-B agrees with ENLIL. However, the SMEI feature had a much more extended radial outflow than shown by ENLIL. This CME was probably driving shock S1 and was associated with CME M1 at VEX and STEREO-B (panels in Figure 5).

Unfortunately, because of the interaction or merger of CMEs 1 and 2, it is unclear whether we can track them as separate entities in the SMEI data. We do not see a clean longitudinally extended, merged structure as shown by ENLIL, but there is an elongated structure, called SM1, stretching between the Earth and the Venus radial. The leading edge of this feature may be the same as the HI-2A-c and SMEI-a fronts revealed by the T–H modelling.

CMEs 3 and 4 are shown as a narrow merged structure by ENLIL. These should correspond to CMEs A and B (using the Harrison *et al.*, 2012 nomenclature), which Möstl *et al.* (2012) suggested are related to the *Wind* features M2 and M3 (which we modelled and discussed in Section 3.2), and the density enhancement around D1 (Figure 4). We noted above that the SMEI features that we call SM2 and SM3 are consistent in timing and location with this density enhancement (Figures 8 and 9). The leading edge of this feature(s) may be the same as the HI-2A-a and SMEI-b fronts revealed by the T–H modelling. On 3 – 4 August there was also a dense structure west of the Earth near 1 AU that is more likely associated with CME 4 (B). This is an extended part of the SMEI SM2, SM3 complex, and it may have arisen from the small western filament eruption (Fil 2) late on 1 August, $\sim 16:00$ UT. If correct, this interpretation of this CME is different from that of Harrison *et al.*, who considered that track B had its origin in the more southern large filament eruption (Fil 3).

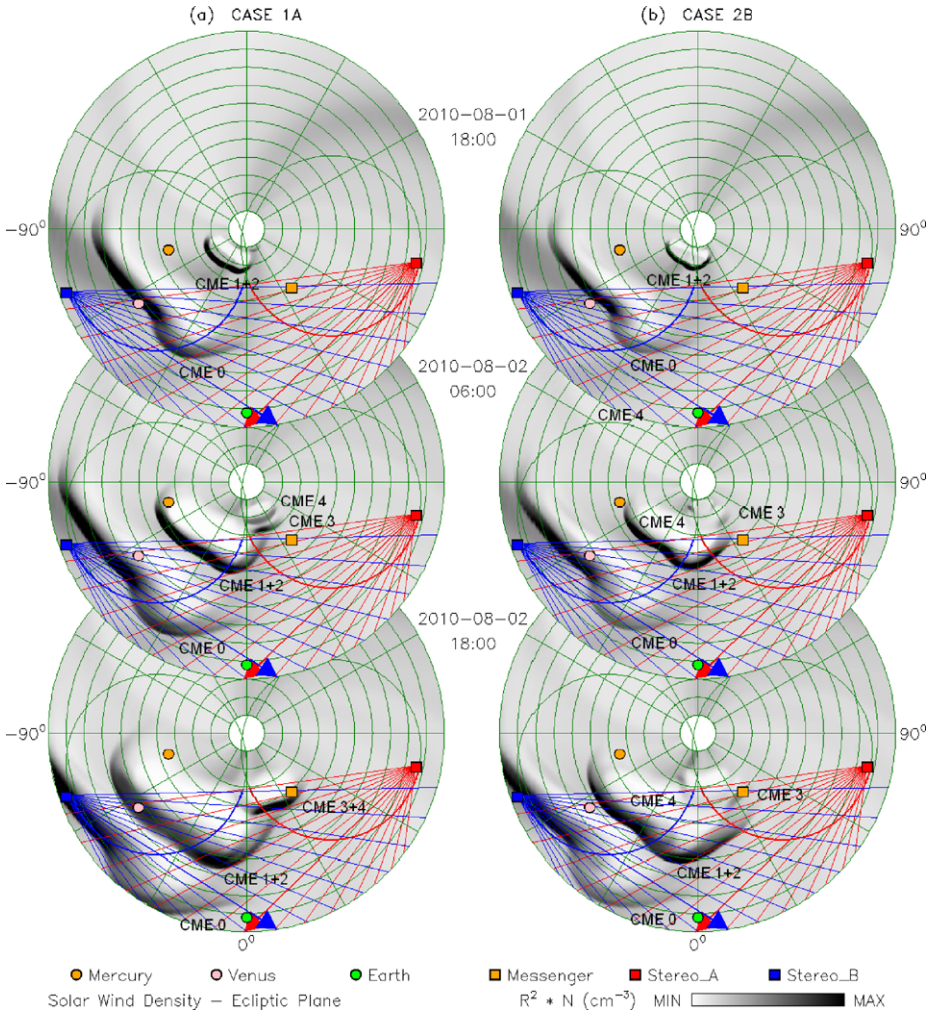

Figure 12 Simulated solar wind density to 1.1 AU in the ecliptic plane runs of Case 1a (left) and Case 2b (right) from Odstrcil *et al.* (2013). Top to bottom panels show results at the times indicated. Density is scaled by $(r/R\ \mathrm{AU})^2$ with the colour scale shown at the bottom. The green rings give heliocentric distance at 0.1 AU intervals. The locations of planets and spacecraft are indicated by the symbols as labelled at the bottom of the figure. The STEREO HI-2 fields of view are shown by light red and blue lines and the viewing direction axes are shown by red and blue arrows. From Odstrcil *et al.* (2013), their Figure 10.

5. Discussion and Conclusions

The late July – early August observations and modelling results demonstrate how nearly simultaneous solar eruptions can immerse up to half of the heliosphere (in terms of ecliptic longitude) with transient material, and emphasise how heliospheric 3D imaging and density reconstructions can be used to understand the trajectories and timing of the plasma flows. This also shows the difficulty in producing a consistent global understanding when only near-Sun imagery and the local information from single-spacecraft measurements are available. We have attempted to develop such a global understanding of the extraordinary

situation of the late July to early August 2010 event series when multiple views near the Sun were available from three 1 AU locations some 70° apart from each other, and *in situ* data were available from five spacecraft spread over 150° in ecliptic longitude and from 0.4 to 1 AU in radial distance. The 3D density reconstructions, based on heliospheric imaging, permit us to "fill in" the temporal and spatial gaps between the near-Sun and *in situ* data to provide a truly global view of the propagation and interactions of the CME plasma as it moved through the inner heliosphere. The results of this study demonstrate the importance of understanding the large scales of CMEs and the space through which they propagate, especially their 3D nature and their interactions with the existing or background structures.

We demonstrated that combining data from the STEREO HI and SMEI heliospheric imaging instruments adds an abundance of information on either a single event or, as in this case, on multiple events. Here we summarise the most important points from this study. The late July – early August 2010 eruptions resulted in a complex pattern of single and mutually interacting plasma and magnetic structures in the inner heliosphere. For the first time these structures could be tracked from their solar origins with the heliospheric imagers on SMEI in Earth orbit and on the twin STEREO spacecraft $\sim 70°$ east and west of the Sun–Earth line, and the existence and timing of the flows and their magnetic structure identified *in situ* at five widely spaced locations. Our study focused on the SMEI observations and 3D density reconstructions, and provides the following new interpretations:

- The 30 July CME (0) propagated just east of STEREO-B, arriving at that spacecraft on 2 – 3 August, and was also detected at Venus (VEX). A shock (S1) passed these spacecraft, trailed by a weak magnetic structure (M1). The ecliptic plane signatures were probably weak because the CME was directed mostly to the north. The structure, SM0, had an extended radial outflow, lasting about 1.5 days, as viewed by SMEI.
- The core of a separate SMEI feature, SM1, tracked west of VEX and 30 – 40° east of the Sun–Earth line and was associated with either or both of CMEs 1 and 2. The SMEI flow past Venus extended over a day, from 2 – 3 August. The time range matched both the shock S2 and the strong trailing magnetic regions, M2 and M3. Since CMEs 1 and 2 began to merge near the Sun, SM1 could have been the massive core of the merged region that was slowed during its passage and did not reach 1 AU until late 4 August. This dense core is also consistent with the outward propagation of the radio emission region localised by direction-finding techniques and considered to be caused by the CME merger (Martinez Oliveros *et al.*, 2012). The T–H model also identified this feature, using both HI and SMEI data. The fast speed of the T–H SMEI-a front was consistent with CME 2, which was the fastest of this series of CMEs.
- The SMEI features SM2 and SM3 were the denser cores of a large band of enhanced density that extended over 50° in longitude from east to west of the Sun–Earth line. Using both HI and SMEI data, the T–H model suggests that this was one large feature that was directed 22° west of the Earth and extended 45° farther toward STEREO-A. The dense cores were aligned along the Sun–Earth axis and matched the time of enhanced density (peaks at D1/D2) *in situ* at *Wind* at L_1. The SMEI density enhancement ranged from late 3 August through 4 August, encompassing the shock (S2) sheath and regions M2 and M3. The M3 structure was a clear magnetic cloud and we modelled it as a high-inclination, left-handed flux rope. The SMEI density was highest just ahead of this flux rope, possibly in a region of interacting CME flows. Although the CME identification of the SMEI structures is uncertain, this extended region was most likely associated with all or parts of CMEs 2, 3, and 4. The T–H SMEI-b front was extended to the west of the Earth and its velocity of 530 km s^{-1} was consistent with that inside the *Wind* M2 and M3 features.

- On 3 – 4 August a part of the SM2, SM3 structures west of the Earth near 1 AU was possibly associated with CME 4 (B). The origin of this feature may have been the small western filament eruption (Fil 2) late on 1 August. Our interpretation of this CME differs from that of Harrison *et al.* (2012), who considered that B had its origin in the more southern large filament eruption (Fil 3).
- The SMEI feature SM4 was a large, dense structure directed mostly west of the Sun–Earth line that did not arrive at 1 AU until early on 6 August. The SMEI-reconstructed density flow at the *Wind* location revealed a second large spike early on 6 August, so the eastern edge of SM4 might have grazed L_1/Earth. However, there was no large increase in the *Wind* density profile, therefore the feature must have passed west of L_1. The T–H model showed that this SMEI structure reached 1 AU at this time and was centred 24° west, and extending mostly north, of the Earth, with a velocity of 985 km s^{-1}. We are not sure of the solar origins of this later SMEI feature, but it could have been related to the eruption of CME 5, the large southernmost filament eruption (Fil 3) late on 1 August. This seems consistent with the passage of M1 by MESSENGER later on 2 August. Möstl *et al.* (2012) concluded that this M1 was part of the same magnetic structure as M3 at L_1/Earth, although they were separated by 50° in longitude. However, the SMEI reconstructions do not show a coherent density structure connecting the MESSENGER location and the Earth.
- We performed force-free, flux-rope modelling and multipoint *in situ*, non-force-free, flux-rope modelling of the *in situ* CME M2 and M3 magnetic structures observed at VEX and STEREO-B. Our model fitted M2 as a small left-handed flux rope with moderate inclination at both spacecraft. However, we cannot be sure whether the M2 structure at VEX and STEREO-B was just the shocked part of the M1 structure, or if it was a separate CME/flux rope.
- For the M3 structures, we achieved flux-rope fits at VEX and STEREO-B that resulted in right-handed structures, while the fit at L_1 showed a different structure with the opposite sign. The rope parameters at L_1 indicate that flux rope was most likely a different structure than those at VEX and STEREO-B. The parameters of the STEREO-B and VEX M3 flux ropes were consistent with their being a single flux-rope structure with a slight bent along its axis between the two spacecraft. In general, our results confirmed those of Möstl *et al.* (2012) for these M3 structures. However, the timing and location of the SMEI structures suggests that the M3 regions at VEX and STEREO-B may not have been physically connected. For example, SMEI showed two different density structures that are not clearly connected.
- The ENLIL results from Odstrcil *et al.* (2013) tend to support the SMEI 3D reconstructions. The timing of the fronts at the spacecraft and the Earth locations were relatively consistent. However, the observed density flows outward from the Sun were longer-lived, more extended in the radial direction, than in the simulations. This is probably due to limitations in the fitting of the hydrodynamic ejecta used to drive the transients in the ENLIL code. Neither did we see evidence that CME 0 extended as far west as the Earth. CMEs 3 and 4 may have been denser and more extensive than in the simulation. The SMEI reconstructions showed a significant enhancement(s) to the west of the Sun–Earth line.

We emphasise the crucial importance of using both observations and models to better understand the structure and propagation of CMEs. The models help us to understand the gross propagation characteristics involved in interplanetary shocks, overall kinematics, and interactions both between one CME and another and with background solar wind structures.

The observations help us to constrain the models and adjust key parameters of the models, such as their initial conditions, geometry, and speed.

Despite this unprecedented collection of data and their analyses, it remains difficult to unambiguously identify exactly which CME was a match to which shock, flux rope, or CME observed *in situ*. If nothing else, the heliospheric density data investigated here show us that the propagation of multiple CME flows with subsequent interactions with each other and with the background solar wind can lead to complex heliospheric structures. On the other hand, our results illustrate that using global imaging techniques, combined with multiple *in situ* measurement sites, adds significant information for interpreting and understanding this complex activity. Our results, along with those from the other papers on these multiple August 2010 events, demonstrate that we need both solar and heliospheric remote-sensing observations as well as *in situ* measurements and modelling to better understand the development and propagation of multiple CMEs.

Acknowledgements We acknowledge the organisers of and the beneficial discussions at the three August 2010 events workshops, held in January 2011 in Abingdon, England, March 2011 in Graz, Austria, and June 2011 in Aberystwyth, Wales, which were vital in producing this paper. The *Solar Mass Ejection Imager* (SMEI) instrument is a collaborative project of the U.S. Air Force Research Laboratory, NASA, the University of California at San Diego, the University of Birmingham, UK, Boston College, and Boston University. The STEREO SECCHI *Heliospheric Imager* (HI) instrument was developed by a collaboration that included the Rutherford Appleton Laboratory and the University of Birmingham, both in the United Kingdom, the Centre Spatial de Liège (CSL), Belgium, and the US Naval Research Laboratory (NRL), Washington DC, USA. The SECCHI project is an international consortium of the Naval Research Laboratory, Lockheed Martin Solar and Astrophysics Lab, NASA Goddard Space Flight Center, Rutherford Appleton Laboratory, University of Birmingham, Max-Planck-Institut für Sonnensystemforschung, Centre Spatial de Liège, Institut d'Optique Théorique et Appliquée, and Institut d'Astrophysique Spatiale. We also benefited from data from the SOHO mission, which is an international collaboration between NASA and ESA, and also from the SOHO/LASCO CME catalog, generated and maintained by the Center for Solar Physics and Space Weather, The Catholic University of America in cooperation with NRL and NASA. The work of DFW was supported at Boston College by Air Force contracts AF19628-00-K-0073 and FA8718-04-C-0006 and Navy contracts N00173-07-1-G016 and N00173-10-1-G001. The work of CM was supported by the European Union Seventh Framework Programme (FP7/2007-2013) under grant agreement no. 263252 (COMESEP), and by a Marie Curie International Outgoing Fellowship within the 7th European Community Framework Programme. MT acknowledges the Austrian Science Fund (FWF): FWF V195-N16. BVJ, JMC, and H-SY were supported by UCSD NSF grants ATM-0852246 and AGS-1053766, NASA grant NNX11AB50G, and AFOSR grant 11NE043. MMB acknowledges support on these analyses from UCSD NSF grant ATM-0925023, and also from a UK STFC Standard Grant to Aberystwyth University for continued CME and heliospheric interplanetary scintillation (IPS) and white-light analyses. TAH was partially supported by the NSF/SHINE Competition (Award 0849916) and the NASA Heliophysics program (grant NNX10AC05G). CJF was supported by NASA grant NX10AQ29G and NSF grant AGS-1140211.

References

Anderson, B.J., Acuña, M.H., Lohr, D.A., Scheifele, J., Raval, A., Korth, H., Slavin, J.A.: 2007, *Space Sci. Rev.* **131**, 417.

Bisi, M.M., Jackson, B.V., Hick, P.P., Buffington, A., Odstrcil, D., Clover, J.M.: 2008, *J. Geophys. Res.* **113**, A00A11. doi:10.1029/2008JA013222.

Burlaga, L.F.: 1988, *J. Geophys. Res.* **93**, 7217.

Burlaga, L., Sittler, E., Mariani, F., Schwenn, R.: 1981, *J. Geophys. Res.* **86**, 6673.

Crooker, N.U., Siscoe, G.L., Shodan, S., Webb, D.F., Gosling, J.T., Smith, E.J.: 1993, *J. Geophys. Res.* **98**, 9371.

Davies, J.A., Harrison, R.A., Rouillard, A.P., Sheeley, N.R., Perry, C.H., Bewsher, D., *et al.*: 2009, *Geophys. Res. Lett.* **36**, L02102.

Davis, C.J., Davies, J.A., Lockwood, M., Rouillard, A.P., Eyles, C.J., Harrison, R.A.: 2009, *Geophys. Res. Lett.* **36**, L08102.

de Koning, C.A., Pizzo, V.J., Biesecker, D.A.: 2009, *Solar Phys.* **256**, 167.

Domingue, D.L., Russell, C.T. (eds.): 2007, *The MESSENGER Mission to Mercury*, *Space Sci. Rev.* **131**, Springer, Netherlands, 624 pp.
Eyles, C.J., Simnett, G.M., Cooke, M.P., Jackson, B.V., Buffington, A., Hick, P.P., Waltham, N.R., King, J.M., Anderson, P.A., Holladay, P.E.: 2003, *Solar Phys.* **217**, 319.
Eyles, C.J., Harrison, R.A., Davis, C.J., Waltham, N.R., Shaughnessy, B.M., Mapson-Menard, H.C.A., *et al.*: 2009, *Solar Phys.* **254**, 387.
Harrison, R.A., Davies, J.A., Möstl, C., Liu, Y., Temmer, M., Bisi, M.M., *et al.*: 2012, *Astrophys. J.* **750**, 45.
Howard, T.A.: 2011, *J. Atmos. Solar-Terr. Phys.* **73**, 1242.
Howard, T.A., Tappin, S.J.: 2009, *Space Sci. Rev.* **147**, 89. doi:10.1007/s11214-009-9577-7.
Howard, T.A., Tappin, S.J.: 2010, *Space Weather* **8**, S07004. doi:10.1029/2009SW000531.
Howard, R.A., Moses, J.D., Vourlidas, A., Newmark, J.S., Socker, D.G., Plunkett, S.P., *et al.*: 2008, *Space Sci. Rev.* **136**, 67.
Hu, Q., Sonnerup, B.U.O.: 2002, *J. Geophys. Res.* **107**(A7), 1142. doi:10.1029/2001JA000293.
Hu, Q., Smith, C.W., Ness, N.F., Skoug, R.M.: 2004, *J. Geophys. Res.* **109**, 3102.
Hundhausen, A.J.: 1993, *J. Geophys. Res.* **98**(A8), 13177.
Jackson, B.V., Buffington, A., Hick, P.P., Altrock, R.C., Figueroa, S., Holladay, P.E., *et al.*: 2004, *Solar Phys.* **225**, 177.
Jackson, B.V., Buffington, A., Hick, P.P., Wang, X., Webb, D.: 2006, *J. Geophys. Res.* **111**, A04S91. doi:10.1029/2004JA010942.
Jackson, B.V., Buffington, A., Hick, P.P., Clover, J.M., Bisi, M.M., Webb, D.F.: 2010a, *Astrophys. J.* **724**, 829.
Jackson, B.V., Hick, P.P., Buffington, A., Bisi, M.M., Clover, J.M.: 2010b, *Adv. Geosci.* **21**, 339.
Jackson, B.V., Hick, P.P., Buffington, A., Bisi, M.M., Clover, J.M., Tokumaru, M., Kojima, M., Fujiki, K.: 2011, *J. Atmos. Solar-Terr. Phys.* **73**(10), 1214. doi:10.1016/j.jastp.2010.11.023.
Kahler, S.W., Webb, D.F.: 2007, *J. Geophys. Res.* **112**, A09103. doi:10.1029/2007JA012358.
Kaiser, M.L., Kucera, T.A., Davila, J.M., St. Cyr, O.C., Guhathakurta, M., Christian, E.: 2008, *Solar Phys.* **247**(1), 171.
Krall, J., St. Cyr, O.C.: 2006, *Astrophys. J.* **652**, 1740.
Lepping, R.P., Acũna, M.H., Burlaga, L.F., Farrell, W.M., Slavin, J.A., Schatten, K.H., *et al.*: 1995, *Space Sci. Rev.* **71**, 207.
Li, T., Zhang, J., Zhang, Y., Yang, S.: 2011, *Astrophys. J.* **739**, 43.
Liu, Y., Davies, J.A., Luhmann, J.G., Vourlidas, A., Bale, S.D., Lin, R.P.: 2010a, *Astrophys. J. Lett.* **710**, L82.
Liu, Y., Thernisien, A., Luhmann, J.G., Vourlidas, A., Davies, J.A., Lin, R.P., Bale, S.D.: 2010b, *Astrophys. J.* **722**, 1762.
Liu, R., Liu, C., Wang, S., Deng, N., Wang, H.: 2010c, *Astrophys. J.* **725**, L84.
Liu, Y., Luhmann, J.G., Bale, S.D., Lin, R.P.: 2011, *Astrophys. J.* **734**, 84.
Liu, Y., Luhmann, J.G., Möstl, C., Martinez-Oliveros, J.C., Bale, S.D., Lin, R.P., Harrison, R.A., Temmer, M., Webb, D.F., Odstrcil, D.: 2012, *Astrophys. J.* **746**, L15.
Lugaz, N., Vourlidas, A., Roussev, I.I.: 2009, *Ann. Geophys.* **27**, 3479.
Lugaz, N., Hernandez-Charpak, J.N., Roussev, I.I., Davis, C.J., Vourlidas, A., Davies, J.A.: 2010, *Astrophys. J.* **715**, 493.
Martinez Oliveros, J.C., Raftery, C.L., Bain, H.M., Liu, Y., Krupar, V., Bale, S., Krucker, S.: 2012, *Astrophys. J.* **748**, 66.
Mierla, M., Inhester, B., Antunes, A., Boursier, Y., Byrne, J.P., Colaninno, R., *et al.*: 2010, *Ann. Geophys.* **28**, 203.
Möstl, C., Farrugia, C.J., Biernat, H.K., Leitner, M., Kilpua, E.K.J., Galvin, A.B., Luhmann, J.G.: 2009a, *Solar Phys.* **256**, 427.
Möstl, C., Farrugia, C.J., Miklenic, C., Temmer, M., Galvin, A.B., Luhmann, J.G., *et al.*: 2009b, *J. Geophys. Res.* **114**, 4102.
Möstl, C., Farrugia, C.J., Temmer, M., Miklenic, C., Veronig, A.M., Galvin, A.B., Leitner, M., Biernat, H.K.: 2009c, *Astrophys. J. Lett.* **705**, L180.
Möstl, C., Temmer, M., Rollett, T., Farrugia, C.J., Liu, Y., Veronig, A.M., Leitner, M., Galvin, A.B., Biernat, H.K.: 2010, *Geophys. Res. Lett.* **37**, L24103.
Möstl, C., Farrugia, C.J., Kilpua, E.K.J., Jian, L., Liu, Y., Eastwood, J., *et al.*: 2012, *Astrophys. J.* **758**, 10.
Mulligan, T.L.: 2002, The structure of interplanetary coronal mass ejections and their solar origins. PhD Thesis, UCLA.
Odstrcil, D., Pizzo, V.J., Arge, C.N.: 2005, *J. Geophys. Res.* **110**, A02106. doi:10.1029/2004JA010745.
Odstrcil, D., Xie, H., de Koning, C.A., Rouillard, A.P., Möstl, C., Temmer, M., et al.: 2013, *J. Geophys. Res.* submitted.
Ogilvie, K.W., Chornay, D.J., Fritzenreiter, R.J., Hunsaker, F., Keller, J., Lobell, J., *et al.*: 1995, *Space Sci. Rev.* **71**, 55.

Pizzo, V.J., Biesecker, D.A.: 2004, *Geophys. Res. Lett.* **31**, L21802. doi:10.1029/2004GL021141.
Rouillard, A.P.: 2011, *J. Atmos. Solar-Terr. Phys.* **73**, 1201.
Rouillard, A.P., Davies, J.A., Forsyth, R.J., Rees, A., Davis, C.J., Harrison, R.A., *et al.*: 2008, *Geophys. Res. Lett.* **35**, L10110. doi:10.1029/2008GL033767.
Schrijver, C.J., Title, A.M.: 2011, *J. Geophys. Res.* **116**, A04108.
Sheeley, N.R. Jr., Walters, J.H., Wang, Y.M., Howard, R.A.: 1999, *J. Geophys. Res.* **104**, 24739 – 24768.
Tappin, S.J., Howard, T.A.: 2009a, *Space Sci. Rev.* **147**, 55.
Tappin, S.J., Howard, T.A.: 2009b, *Astrophys. J.* **702**, 862. doi:10.1088/0004-637X/702.
Temmer, M., Vrsnak, B., Rollett, T., Bein, B., de Koning, C.A., Liu, Y., Bosman, E., Davies, J.A., Möstl, C., Zic, T., Veronig, A.M., Bothmer, V., Harrison, R., Nitta, N., Bisi, M., Flor, O., Eastwood, J., Odstrcil, D., Forsyth, R.: 2012, *Astrophys. J.* **749**, 57.
Török, T., Panasenco, O., Titov, V.S., Mikić, Z., Reeves, K.K., Velli, M., Linker, J.A., De Toma, G.: 2011, *Astrophys. J. Lett.* **739**, L63.
Vourlidas, A., Howard, R.A.: 2006, *Astrophys. J.* **642**, 1216.
Wood, B.E., Howard, R.A.: 2009, *Astrophys. J.* **702**, 901.
Wood, B.E., Howard, R.A., Socker, D.G.: 2010, *Astrophys. J.* **715**, 1524.
Wu, C.-C., Dryer, M., Wu, S.T., Wood, B.E., Fry, C.D., Liou, K., Plunkett, S.: 2011, *J. Geophys. Res.* **116**, A12103. doi:10.1029/2011JA016947.
Xie, H., St. Cyr, O.C., Gopalswamy, N., Yashiro, S., Krall, J., Kramar, M., Davila, J.: 2009, *Solar Phys.* **259**, 143. doi:10.1007/s11207-009-9422-x.
Zhang, Y., Du, A.M., Feng, X.S., Sun, W., Fry, C.D., Deehr, C.S., Dryer, M., Zieger, B.: 2013, *Solar Phys.* in press.
Zurbuchen, T.H., Richardson, I.G.: 2006, *Space Sci. Rev.* **123**, 31.